Chem Soc Rev

Development in spontaneous and coherent Raman scattering microscopic imaging for biomedical applications

Journal:	*Chemical Society Reviews*
Manuscript ID	CS-REV-07-2015-000564.R1
Article Type:	Review Article
Date Submitted by the Author:	25-Sep-2015
Complete List of Authors:	Krafft, Christoph; Institute of Photonic Technology, Schie, Iwan; Leibniz Institute of Photonic Technology, ; Meyer, Tobias; Institute of Photonic technology, Schmitt, Michael; Friedrich-Schiller-Universitat Jena, Institut fur Physikalische Chemie Popp, Jürgen; Leibniz Institute of Photonic Technology,

Chemical Society Reviews

Review

Developments in Spontaneous and Coherent Raman Scattering Microscopic Imaging for Biomedical Applications

Received 00th January 20xx,
Accepted 00th January 20xx

DOI: 10.1039/x0xx00000x

www.rsc.org/

C. Krafft,[a]† I.W. Schie[a]†, T. Meyer[b]†, M. Schmitt[b] and J. Popp[a,b]

First, the potential role of Raman-based techniques in biomedicine is introduced. Second, an overview about the instrumentation for spontaneous and coherent Raman scattering microscopic imaging is given with a focus of recent developments. Third, imaging strategies are summarized including sequential registration with laser scanning microscopes, line imaging and global or wide-field imaging. Finally, examples of biomedical applications are presented in the context of single cells, laser tweezers, tissue sections, biopsies and whole animals.

1. Why Raman-based techniques in biomedicine?

Cells and tissues are characterized by a specific dynamic biochemical composition and molecular structure. In a similar way, each pathology or cellular abnormality is accompanied by biochemical and molecular changes, which may also be dynamic in nature. Optical and spectroscopic techniques that correlate the biochemical composition, molecular structure, and its variations with the diagnosis would provide powerful clinical tools. A variety of optical techniques have been suggested as a means of imaging in biomedicine, and each of them has certain advantages, disadvantages and limitations. To name a few, confocal fluorescence microscopy and photoacoustic imaging rely upon the specific uptake of dyes. Offering high sensitivity, specificity and speed, dyes might be unevenly distributed in cells or tissues and might be toxic. Label-free imaging techniques such as infrared microscopy (IR), optical coherence tomography (OCT), confocal reflection (CR), two-photon excited fluorescence (TPEF), second harmonic generation (SHG) and third harmonic generation (THG) imaging have also been proposed. OCT, CR and THG reveal morphological features but lack chemical contrast for differential diagnosis. IR microscopy probes molecular vibrations providing chemical contrast, but spatial resolution is inferior due to longer wavelength in the mid-IR from 2.5 to 10 µm. SHG and TPEF microscopy primarily highlight collagen and auto-fluorescent species, respectively, and both signals can be weak or absent in some specimens. This contribution focuses on Raman-based techniques that fulfil the requirements of label-free biomedical imaging with following advantages: (i) molecular vibrations of all constituents are probed simultaneously without external labels proving a specific molecular fingerprint; (ii) this information can be obtained at various excitation wavelengths and intensities that are non-destructive to living organisms, and can be tuned with resonance measurements to specific chemical species; (iii) implementation as microscopic technique is capable of imaging molecular species at submicrometer resolution, as well as the ability to collect images as a function of depth as well as space; (iv) coherent Raman scattering (CRS) is coupled to rapid laser scanning microscopes to collect images at video-rates and (v) CRS can be combined with other multiphoton techniques to improve chemical contrast. The potential of Raman-based techniques in clinical diagnostics has been proven in many reports that include also combining the benefits of complementary techniques mentioned above. The collection of papers in this topical issue will give an overview of instrumental developments and examples of biomedical applications. Comprehensive reviews have recently been given in the context of Raman spectroscopy for biomedical analysis,[1] CRS microscopies for clinical and biological studies,[2] and molecular pathology via Raman and infrared spectral imaging.[3]

Furthermore, linear and non-linear Raman approaches have been combined within the last years with other optical and spectroscopic imaging techniques (fluorescence, SHG, THG, OCT etc.) in a multimodal approach for biomedical imaging. Such a combination of Raman with different contrast phenomena in one microscopic setting is very beneficial for improving the diagnostic result of Raman spectroscopy.[4]

1.1 Early developments

In the last 30 years Raman microspectroscopy has made a giant leap forward from being a niche technology in analytical chemistry to a broadly available tool of choice for label-free sample analysis.[5] These improvements are highlighted by comparison of more recent reports as shown below and older reports, e.g. *Abraham et al.* in 1979.[6] The researchers used a state-of-the-art custom-build Raman microspectrometer to investigate biological material, such as the cytoplasm of multinucleated giant cell of the lymph nodes. The acquisition for a single Raman spectrum from that sample was about 150 min.; while the acquisition of hyperspectral Raman images was

[a] *Leibniz Institute of Photonic Technology Albert-Einstein-Str. 9, 07745 Jena, Germany.*
[b] *Institute of Physical Chemistry and Abbe Center of Photonics, Friedrich-Schiller-University Jena, Helmholtzweg 4, 07743 Jena, Germany.*
† Footnote: Authors contributed equally.

not imaginable. *Erz et al*. mentioned in their review on Raman spectroscopy[7] from 1980, that for some samples it should technically be possible to acquire Raman spectra in a few seconds. Due to the enormous developments in laser, detector and filter technology, today, 35 years later, high-quality Raman spectra are routinely acquired from biological samples in less than a second.

1.2 Current state of knowledge

Improved diagnostic methods are needed in various clinical fields. In the past decade, Raman spectroscopy has evolved as a versatile bioanalytical tool enabling label-free, chemically and spatially resolved assessment of cells and tissues at molecular level. Numerous research groups have reported proof of concept studies demonstrating the potential of Raman microscopic imaging in cytopathology and histopathology. Raman-based methods can probe biomolecules such as proteins, lipids, nucleic acids and carbohydrates within complex matrices without preparation, even under *in vivo* condition. The physical mechanism behind Raman spectroscopy is inelastic light scattering of monochromatic laser radiation from molecules. As Raman signals of most biomolecules are relatively weak, intense excitation lasers and sensitive detection schemes are used. If the laser wavelength is within the absorption range of molecules, the red shifted portion of the Raman spectrum (Stokes signal) can overlap with fluorescence emission. As near infrared excitation (as does excitation in the deep ultraviolet (UV)) shows low absorption for most biomolecules, unwanted contributions from associated fluorescence are minimal.

1.3 Outline to respond to the unmet clinical needs

This contribution describes state-of-the art techniques in Raman microscopic imaging and current developments to apply Raman based methods to unmet clinical needs and translate them into the clinic. Further developments include (i) improved laser sources for excitation, (ii) dedicated microscopy techniques that enable automated imaging, (iii) higher sensitivities down to sub-second exposure time per spectrum, (iv) image acquisition times of few minutes, and (v) objective classification routines for diagnosis of cells and tissues based on Raman data. Because of the complexity of the latter topic, it will not be covered here and illustrative examples will be given instead. Like any microscopic imaging modality, spontaneous Raman and CRS microscopic modalities would generate field of views (FOVs) that are smaller than clinical specimens (tissue sections, biopsies, surgical cavity…). Consequently, protocols need to be developed to combine and complement existing methods. The fact that images can only be collected at a maximal depth of penetration of approximately 100 µm (confocal spontaneous Raman) and 500 µm (CRS) also needs to be considered.

2. Instrumentation for spontaneous Raman microscopic imaging

A scheme of spontaneous Raman scattering is shown in figure 1. A similar scheme for coherent Raman scattering will be presented at the beginning of section 3. Because Raman signals of most biomolecules are weak, Raman microscopic systems for biomedical applications are optimized for efficient excitation and collection of inelastically scattered light. The main components that have not significantly changed in the last two decades [8] are lasers, which are coupled into microscopes, and spectrometers with multichannel detectors for registration of Raman spectra. These components together with their recent progress are separately described in this section. A more detailed introduction into practical Raman spectroscopy is given in a recent textbook.[9]

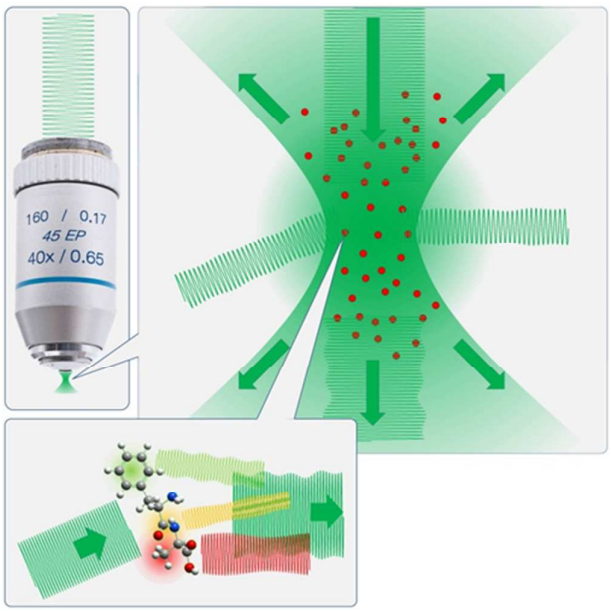

Figure 1: Scheme of spontaneous Raman scattering. The sample is illuminated by a continuous wave laser generating a small amount of Raman scattering upon excitation of molecular vibrations. The emission is like that of a Hertzian dipole and all Raman active vibrations generate scattering, which adds to the total Raman spectrum. Raman scattering is induced throughout the beam path.

2.1 Lasers

In general, lasers are ideal excitation sources for Raman spectroscopy because of their intense, monochromatic and small divergence, polarized and coherent emission. Particular properties of excitation lasers in Raman spectroscopy are wavelength stabilization and narrow bandwidth. The band width of the excitation laser determines the minimum width of Raman bands that can be correctly measured. For biological samples in liquid or solid phase this requirement means that the band width should be less than 10 cm^{-1} (typically even smaller than 1 cm^{-1}) as most bands have inherent full width at half maximum (FWHM) above 10 cm^{-1}. As the position of Raman bands depend on the position of the excitation

wavelength, variations will also change the wavenumber of Raman bands. Calibration procedures use the wavenumber of well-known Raman scatterers such as the cyclohexane band at 801.3 cm^{-1} to set the wavenumber of the excitation laser to zero. The standard Raman spectra of eight materials including cyclohexane were compiled by the McCreey research group [10].

If the sample is transparent and non-absorbing which is the case in gas sensing high intensities of more than 1 W can be applied. In the biomedical context this has been reported for breath analysis [11]. Here, FWHMs are found below 10 cm^{-1}. But this is less relevant for the current topic microscopic imaging. For cell and tissue samples laser intensity must be kept below the damaging threshold to avoid carbonization and phototoxicity in *in vivo* studies. These unwanted effects also depend on the wavelength, the optical geometry which determines the focus size, and the cell or tissue type. Typical laser powers at the sample are in the range of 10 to 100 mW.

Whereas the wavenumber of Raman bands is independent of the wavelength of the excitation laser, the scattering intensity is not. According to the Rayleigh law, $2^4 = 16$ fold more intense scattering is observed if a VIS laser at 532 nm is used instead of a NIR laser at 1064 nm for the same excitation power. This factor further increases to $4^4 = 256$ for a UV laser at 266 nm. The Raman scattering cross sections of molecular vibrations also depends on the wavelength. If the excitation wavelength is close to electronic absorption, then the Raman cross section is enhanced due to a resonance effect. Common electronic absorption occurs below 230 nm for peptide bonds and aromatic amino acids in proteins, near 260 nm for nucleobases and phenylalanine, near 280 nm for tyrosine and tryptophan, for porphyrin groups near 440 and 550 nm in e.g. hemoglobin of red blood cells (erythrocytes), for cytochrome C near 520 and 550 nm in mitochondria, and throughout the visible range for melanin e.g. in pigmented skin and nevi. In case of electronic absorption, the damaging threshold is low, the sample is prone to decomposition, the laser intensity and exposure time should be reduced, and the Raman signal might overlap with fluorescence emission.

Popular wavelengths in Raman spectroscopy are 488 and 514 nm emitted by argon ion lasers, 413 and 647 nm by krypton ion lasers, 532 and 1064 nm by solid state Nd-YAG lasers, 633 nm by helium neon lasers, and 785 nm by diode lasers. Diode lasers are available for many excitation wavelengths from 660 to 880 nm and became very popular in the last years due to compact size, good performance to price ratio and user-friendly operation compared to gas lasers that need water cooling for high intensity versions. Laser line filters are narrow bandpass filters that suppress plasma lines in gas lasers or ASE radiation in diode lasers. Thus, the laser beam is “cleaned” and possible signals with other wavelengths are removed. NIR lasers are chosen in most biomedical studies because electronic absorption and associated fluorescence background are reduced, and penetration of radiation is maximized.

Shifted excitation and modulated excitation Raman spectroscopy are approaches to separate overlapping fluorescence from Raman signals. As described above, the Raman bands shift as a function of the excitation wavelength whereas the broad fluorescence emission remains largely unchanged. Algorithms have been developed to extract the Raman bands from data sets collected at slightly shifted wavelengths (1 to 2 nm) [12]. It has been reported that background from other constant signals e.g. ambient light can also be suppressed in this way.[13] Fluorescence suppression techniques in Raman spectroscopy were reviewed[14].

2.2 Microscopes

Coupling of Raman spectrometers with microscopes combines the advantages of maximum photon density for excitation and maximum photon collection using high numerical aperture objective lenses. Lasers and Raman detection systems can be conveniently coupled with microscopes by optical fibers which combine high stability, flexibility and throughput. If the microscopes are installed in a shielded chamber, they can be operated at ambient light and fulfil the laser safety class 1. As most research-grade microscopes can be adapted for Raman spectroscopic use, all options are available such as epi (= illumination through the objective) and dia (= illumination through the condenser) illumination with CCD cameras for visible inspection, upright or inverted geometry, motorized x-y-z translational stage for imaging and autofocus (see section 4) and full range of microscope objective lenses. Depending on the application, this includes objective lenses with improved transmission in the UV or NIR range, water or oil immersion objective lenses with or without cover glass correction. A pinhole in the detection light path determines the confocality of microscopes. The core of the collection fiber acts already as pinhole. A smaller pinhole further improves the confocality at the expense of the signal throughput. Coupling of single-mode lasers into single mode excitation fibers enable a minimum laser spot size for best lateral and axial resolution.

For special applications scanning near field optical microscopes (SNOM) and atomic forces microscope (AFM) have been coupled with Raman systems[15]. If the AFM tips are functionalized with plasmonic nanoparticles, so called tip enhanced Raman scattering (TERS) provides sub-diffraction limited resolution[16]. However, these topics are not within the scope of the current contribution and the interested reader is referred to reviews for further information[17].

2.3 Spectrometers

The dispersive element in spectrometers used in Raman systems is usually a grating whose line density determines the spectral resolution and spectral coverage together with the size of the entrance slit, the distance between grating and detector (focal length of the spectrometer) and the pixel size of the CCD detector (see next paragraph). Because the wavenumber is reciprocal of the wavelength, the wavenumber axis is not linear. That means for the Stokes shifted portion of the Raman spectrum, a detector pixel closer to the excitation wavelength corresponds to a larger wavenumber range than pixels at higher wavelengths. Interpolation routines have been developed for linearization. The wavenumber axis needs to be calibrated by assigning Raman wavenumbers (in cm^{-1}) to pixel numbers. For such a calibration a light source with known

emission lines or a compound with known Raman bands can be used. Narrow band plasma lines of gas lasers that can be detected after removing the laser line filter have been recommended to calibrate the wavenumber axis of spectrometers[18]. Accessories that generate narrow gaseous emission lines are also available for calibration purposes. Alternatively, Raman bands of standards compounds with well-documented positions allow wavenumber calibration. More details have been published[19].

Spectrometers in Czerny Turner design use reflective gratings. A turret accommodates low resolution grating for large spectral coverage and high resolution grating for smaller spectral coverage. Efficient coupling is achieved if the f-number of the spectrometer is adapted to the numerical aperture of the collection fiber. Low f-numbers are realized by lens-based spectrometers. However, the aberrations of lenses are only corrected for limited wavenumber intervals. Transmissive holographic gratings combine two gratings in one optical element[20]. The first grating disperses the low wavenumber range onto one portion of the CCD detector, whereas the second grating is slightly tilted and disperses the high wavenumber range onto another portion of the CCD detector. Both ranges are combined to a full spectrum with approximately twice the spectral resolution compared to a single low resolution grating for the same spectral coverage. In the past years, volume phase gratings (VPG) became popular, in particular for compact spectrometers. VPG consists of a volume with a periodically change in the refractive index. Depending on the orientation of the modulation of the refractive index, VBG can be used to either transmit or reflect a small bandwidth of wavelengths. Bragg's law adapted for volume hologram dictates which wavelength will be diffracted. The limitation of transmissive holographic gratings and VPG is that they are more expensive than reflective gratings and they are designed for a single excitation wavelength. Because such gratings are mounted in a fixed position, they offer high stability. The impact of volume phase holographic filters and grating on the development of Raman instrumentation was previously reported[21].

2.4 Detectors

Charge coupled device (CCD) cameras are multichannel detectors that register the Raman spectrum. If the spectral coverage is smaller than the full spectrum, more than one CCD exposure at different grating positions are collected and subsequently combined to a single spectrum. Beside the spectrometer specifications, the spectral coverage depends on the number of pixels, and the wavenumber interval per pixel depends on the pixel size. Common pixel numbers for the spectral dimension are between 1024 and 2048 each 10-26 µm in size. If a laser spot is dispersed on the CCD, only few pixels will be required in the second, lateral, dimension and the pixel number will be generally lower (1 to 400, see also figure 7 in section 4.2). The illuminated pixels along the lateral dimension are binned for registration and the non-illuminated are not registered as they only contribute to the noise. Different imaging strategies have been developed in the past to utilize more pixels in the lateral dimension (see chapter 4). The sensitivity of a CCD detector which is indicated by the quantum efficiency (QE = the number of electrons generated per photon) is wavelength dependent. The intensity axis can be calibrated using a white light source with a continuous and known emission spectrum to compensate the response curve of the detector (QE as function of the wavelength) and slight variations in pixel sensitivities. It is not only important to have a high QE, but also the dark signal should be as low as possible. This dark signal is formed by spontaneous (thermal) generation of electron-hole pairs in the semiconductor detector, and involves the introduction of noise. The dark noise is reduced by cooling. The dark signal (average number of electrons generated in the detector if the detector is not exposed to light) can be compensated by subtracting a dark spectrum from the sample spectrum. Small, handheld Raman instruments are often equipped with uncooled CCD detectors with one row of pixels. A drawback is that dead or hot pixels cannot be corrected. An optimum compromise between low dark noise and sensitivity is achieved at temperatures between -65 and -95 °C. This can be realized by liquid nitrogen cooling down to -196°C plus controlled heating or thermoelectric cooling. To avoid condensation issues, cooled CCD chips are hermetically vacuum sealed.

Different detector geometries have been developed for UV, VIS and NIR wavelength ranges. Front illuminated open electrode configurations have maximum QE near 50%. The back illuminated deep depletion configuration offer higher QEs of more than 90% from the visible to the NIR range. However, the dark noise is higher than for open electrode CCDs and etaloning effects might occur and need correction. The QE dramatically drops towards the band gap of the detector material – the semiconductor silicon – that corresponds to wavelengths near 1100 nm. This is one reason for the choice of 785 nm as excitation wavelength. Then the full Raman spectrum from 0 to 3500 cm^{-1} lies in the wavelength interval from 785 to 1082 nm which is covered by silicon based CCDs. With 1064 nm excitation lasers, indium gallium arsenide detectors are used in dispersive spectrometers and germanium detectors with interferometric Fourier transform detection schemes.

Because the Raman signals as a result of inelastic scattering is several orders of magnitude weaker than the elastic Rayleigh scattering, Holographic Notch filters or dielectric longpass filters suppress the elastically scattered light of the excitation laser, improve the dynamic range of the detectors and reduce the shot noise for better signal to noise ratios. These filters differ in optical density (typically between OD 4 and 6) and bandwidth. A small bandwidth allows collecting Raman bands in the low wavenumber range close to the excitation wavelength. Recently, VPGs were introduced for efficient elastic scattering suppression at high transmission and Raman spectra were collected down to 10 cm^{-1} [22]. In former times, this performance could only be achieved with high resolution double or triple monochromators at the expense of higher costs and higher Raman signal losses.

Electron-multiplying CCDs (emCCDs) were recently introduced for Raman microscopic imaging[23]. The advantage to amplify the Raman signal above the background noise level is particular effective for weak signal levels and at short exposure times in the millisecond range. The contrast and signal-to-noise ratio can be improved by repeated image acquisition. Advancement in the context of detectors for Raman spectroscopy might arise from the application of CMOS sensors. Such an active pixel sensor consists of an integrated circuit containing an array of pixel sensors, each pixel containing a photodetector an active amplifier. The name is derived from the construction technology – complementary metal-oxide-semiconductor (CMOS) – has emerged as an alternative to CCD image sensors. They offer advantages in readout speed that has been demonstrated in time-gated Raman measurements with short laser pulses for fluorescence suppression[24].

3. Instrumentation for coherent Raman scattering

While spontaneous Raman scattering has been extremely successful in identifying disease related chemical changes, that are considered as novel endogenous diagnostic markers, visualizing the distribution of such a molecular marker across large tissue areas by spontaneous Raman scattering is far too time consuming for biomedical routine diagnostics due to the long integration times on the order of seconds per spectrum.

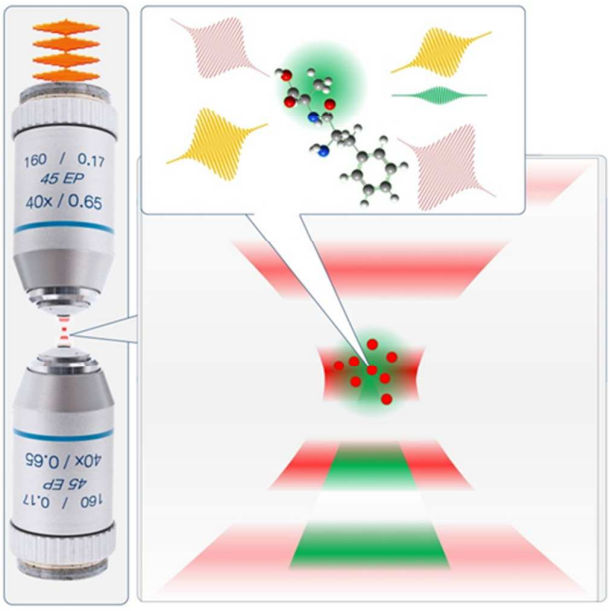

Figure 2: Scheme of coherent Raman scattering (CRS). The sample is illuminated by short laser pulses of two wavelengths exciting a specific vibration by stimulated Raman scattering, which results in Raman loss of the short wavelength pump laser and Raman gain of the long wavelength Stokes laser. Additional coherent scattering of the excited molecules generates CARS and CSRS (anti-Stokes Raman scattering – CARS, coherent Stokes Raman scattering – CSRS, not depicted). CRS is mostly excited in the laser focus where light intensities are highest and the signals are directional.

Here, CRS imaging provides a significant speed advantage enabling real-time visualization of a single Raman marker band with video rate image acquisition speed. [25, 26] Key differences of CRS are depicted in figure 2. Due to its nonlinear intensity dependence, the CRS signal generation is confined to the laser focus and requires pulsed laser excitation in order to reduce the average power at the sample at high peak powers. The most common implementation of single band CRS (see figure 12 in section 4.6) visualizes the spatial distribution of a single Raman active vibration. Today three major implementations of CRS imaging are used: coherent anti-Stokes Raman scattering (CARS)[27], stimulated Raman scattering (SRS) [28, 29] and – most recent – the Raman induced Kerr effect (RIKE),[30-32] which is, however, less suited for biomedical imaging of intact tissue, since the polarization is scrambled during propagation in tissue. A major difference between CARS and SRS results from the fact, that both the concentration dependence and the spectral line shape of single band SRS are identical to spontaneous Raman. CARS signals differ from spontaneous Raman due to the nonlinear concentration dependence and the distortion of the spectral line shape due to interference with nonresonant background signals from four wave mixing. The schemes are depicted in figure 4 in section 3.2. However, the speed advantage of CRS comes at the cost of a significantly enlarged experimental complexity, particularly the need for synchronized ultra-fast lasers and laser scanning microscopes (LSM). Ongoing technical progress particularly in laser technology utilizing optical fibers will fuel the widespread application of CRS in life sciences and as a tool for imaging in biomedicine.[33] Additionally CRS imaging requires more sophisticated routines for data acquisition and processing in order to extract reproducibly the relevant information, i.e., the concentration of the marker. Therefore many efforts focus on the development of image processing routines for CRS data, e.g., for tissue grading.[34-37] Thus, fully automated software tools for online data analysis seem to be possible in the future. Since reinventing CARS microscopy using collinear beam geometry in 1999 significant progress has been made in terms of sensitivity and speed.[27] In particular, the improvement in speed is essential to study molecular dynamics in living systems. Meanwhile, this improvement comes at the price of focusing the excitation energy at a single frequency or within a narrow spectral window. For single frequency excitation, a speed of 100 ns per pixel has been reached.[25, 26, 38] For multiplex excitation of SRS in a spectral window of a few hundred wavenumbers, microsecond per pixel is reached,[39] while the complete spectrum can be acquired within 3.5 ms.[40] These features allow high-speed imaging of dynamics and high throughput single cell analysis. However, in order to realize routine application in biomedicine, technical barriers must still be overcome. Easy-to-use, compact and reliable instruments are needed. In the following we therefore focus on technological developments, specifically laser sources, detectors and detection methods. The text is structured as follows: first we briefly summarize the mechanism of the different realizations of CRS emphasizing their impact on the detection and excitation before we discuss in detail technical

developments, in particular laser sources and detection mechanisms.

3.1 Laser sources for CRS

3.1.1 Laser parameters for CRS

The laser sources used for CRS to date are either a single but spectrally broadband laser source in combination with pulse shaping[41-46] or interferometric techniques.[47] Impulsive stimulated Raman scattering is generated by a train of pulses, which can be achieved either by pulse shaping[41-46] or recently by using laser frequency combs,[48] which is discussed in section 3.1.3. For biomedical applications most CRS approaches require two actively or passively synchronized ultra-short lasers of tunable frequency difference that renders the light source for CRS not only significantly more complex than that required for spontaneous Raman (see section 2.1), which is in general a continuous wave (cw-) laser, but also more demanding than lasers for other multiphoton microscopies, i.e., second or third harmonic generation and multi photon fluorescence. In addition, CRS for biomedical application requires specific laser parameters for efficient signal generation in tissue due to the physical process of CRS as well as distinct properties of tissue. Since there are in general spectrally broadband and narrow imaging schemes for CRS imaging, which will be discussed in depth in section 4, we will include the technique the laser source is intended to be used for. Therefore, suitable laser parameters will be briefly summarized in the following, with emphasis on hyperspectral CRS, i.e., the subsequent detection of images at specific Raman resonances.

The common strategy to (i) efficiently generate nonlinear signals while (ii) keeping the average power at the sample well below the threshold of photodamage is to employ pulsed illumination. Pulsed lasers provide high peak powers on the ~kW level, which is tolerable for sub ns illumination times, while the average power at the sample is only 30 mW.[49-54] While sub-ps pulses provide for the same average power higher peak intensities, their spectral bandwidth exceeds the width of a single Raman transition. In case of SRS spectral intensity off the Raman resonance does not result in the generation of SRS signals. In case of CARS it is even worse: the ratio of resonant to nonresonant signal is reduced, when the spectral width of the pulses exceeds the width of the Raman band.[55] This is due to the fact that for constant spectral intensity, the contrast deteriorating nonresonant background signal increases linearly with the spectral width of the pulse, while the resonant signal saturates, when the convolution of the spectral width of both lasers coincides with the spectral width of the Raman resonance.[55] Hence, for a fixed laser bandwidth, the ratio of resonant to nonresonant CARS signal is fixed, and for narrow bandwidth, this ratio can be high. Hence, for general application a spectral width corresponding to narrow Raman resonances on the order of 1 cm^{-1} should be employed, while for standard application such as to image intense and spectrally broad resonances within the CH-stretching spectral region, 10 cm^{-1} are sufficient. The pulse repetition rate of the laser on the other hand should enable to acquire images at the shortest pixel dwell time required, which is on the order of 100 ns for video rate image acquisition, i.e., 30 frames per second at 512 x 512 pixels, while for most laser scanning applications 1 µs pixel dwell time is sufficient. This corresponds to minimal pulse repetition rates of 1 MHz or 8 MHz for video-rate imaging. [25, 26, 38] However, also the laser noise should be considered, which is crucial in case of modulation transfer signal detection as required for SRS and heterodyned detection of RIKE and CARS. Since the relative intensity noise (RIN) of lasers is lower at higher frequencies and usually approaching the shot noise limit above 1 MHz, high frequency modulation above 1 MHz is beneficial for low noise and fast SRS. Hence, when high frequency modulation in the order of 10…20 MHz is employed for Lock-In detection of SRS signals, laser repetition rates of twice the modulation frequency, i.e., 20…40 MHz, are required. The laser power at the sample is limited by linear and nonlinear photo-induced sample damage. Linear photodamage is due to absorption and heat dissipation, while the dominant nonlinear damage mechanism for imaging tissue is due to two photon absorption. Both strongly depend on the absorption properties of the tissue, thus the damage thresholds varies across different types of tissue. Hence, the laser power needs to be adjusted to the sample of interest, but in general the highest tolerable powers for video-rate imaging are up to 180 mW using a high NA-objective,[26] while even higher powers up to 250 mW have been reported.[56] While the discussion of the tolerable total power at the sample including its dependence on pixel dwell time, tissue absorption, excitation wavelength and pulse duration is beyond the scope of this article, the laser source for CRS imaging should provide the average power of 200 mW per beam to account for optical losses in the microscope and other optical equipment, e.g., optical modulator and optics for beam alignment. Output powers beyond that are not needed, since sophisticated methods for power adjustment are required. This is due to the fact, that reducing the average power by neutral density filters lowers the nonlinear CRS signals drastically, which is why pulse picking in order to lower the average power while maintaining the peak power and nonlinear signal yield per pulse is preferential, but also more difficult to realize.

For imaging different marker molecules tuning the frequency difference of pump and Stokes laser is required. Most important is the spectral coverage of the CH-stretching region from 2750 to 3000 cm^{-1} enabling fastest imaging and discrimination of proteins and lipids,[57] while imaging the OH vibration enables to visualize water diffusion processes.[58-60] Vibrational labelling requires imaging around 2050 – 2150 cm^{-1} using alkyne and deuterium for labelling,[56, 61-64] while the fingerprint spectral region enables label-free imaging of proteins by the amid I band at 1655 cm^{-1} or DNA at 785 cm^{-1}.[65] In summary, the following list of laser parameters is useful for CRS imaging:

- Repetition rate > 1 MHz
- Wavelength 700-1100 nm
- Tuning range 0-3500 cm^{-1}
- Spectral pulse width < 10 cm^{-1}

- Pulse duration <<1ns
- Average power of pump and Stokes laser ~200mW per beam

3.1.2 Solid state lasers for CRS

Lasers for CARS as the oldest realization of CRS imaging have evolved from dye lasers[66] to Titanium-Sapphire (Ti:Sa) lasers pumping optical parametric amplifiers (OPA) or optical parametric oscillators (OPO) at 250 kHz-repetition rate when introducing CARS microscopy using a collinear illumination scheme and high numerical aperture objective lenses.[27] For imaging applications, higher repetition rate lasers need to be used, i.e., lasers of several MHz repetition rate. Here synchronized Ti:Sa-Lasers (i) offer the widest spectral tuneability of laser materials from 700-1000 nm, (ii) allow accessing the full Raman spectrum from 0-4000 cm^{-1}, (iii) provide high peak and average power and finally (iv) are available with pulse durations from 100 fs to a few ps. However, tight synchronization of two independent lasers is challenging. For this purpose the laser signals are monitored at the fundamental pulse repetition rate and at a higher harmonic frequency. The fundamental frequency is used for coarse alignment, while the high harmonic signal allows to precisely lock the phase of two fs or ps-oscillators. The whole system is complex and requires fast and precise motion of several mirrors within the cavity.[67-69] Obviously active synchronization is difficult to maintain for long measurements, rendering passive synchronization as used in OPAs or OPOs beneficial. While first OPAs and OPOs were suffering from low conversion efficiencies when pumping with the SHG of a Ti:Sa-Laser in the UV,[70] highly efficient sources were developed utilizing either SHG of a ps Nd-Vanadate laser at 532 nm or the Ti:Sa-Laser emission directly for OPO pumping.[25, 71-73] Commercially available laser-OPO systems provide a tuning range of 700-4000 cm^{-1}, several 100 mW average power for signal and idler, 80 MHz repetition rate for fast imaging application and high spectral resolution of 3.5 cm^{-1}.[25] Therefore these sources are currently state of the art. Nevertheless, there are demanding and exciting applications requiring two separate synchronized lasers, as described in the following.

3.1.3 Highlight - Frequency comb CRS

By using two synchronized frequency comb lasers coherent Raman spectra covering 200-1400 cm^{-1} can be simultaneously measured within 14.8 µs at 4 cm^{-1} spectral resolution. This approach enables to detect all spectral elements over a wide bandwidth and with high resolution on a single photodetector without moving parts. CARS spectra covering 1200 cm^{-1} containing 300 spectral points and a maximum SNR of 210 have been recorded within 14.8 µs, and imaging has been demonstrated. The method is limited by the refresh rate of the interferogram to 50 pixels / second.[48] Still, high costs, instrument size and alignment issues are a serious concern for routine use of these lasers. Therefore research has focused on the development of more compact sources, which do not need regular maintenance.

3.1.4 Hybrid systems based on solid state lasers and optical fibers

One strategy is to use compact and maintenance free fiber lasers to pump a standard OPO-system in order to reduce the size and to increase the overall conversion efficiency.[74] OPOs pumped by Yb fiber lasers are commercially available.[75] Instead of using a fiber laser to pump an OPO, alternatively passive optical fibers can be used to substitute the OPO for frequency conversion. Here, nonlinear frequency conversion processes in these fibers are employed in order to generate spectrally separated emission wavelengths, which are inherently synchronized to the pump laser. Multiple fiber based frequency conversion processes can be employed: supercontinuum (SC) generation,[76, 77] soliton self frequency shift (SSFS) [78, 79] and four wave mixing (FWM).[80, 81] Photonic crystal fibers (PCF) are due to their high nonlinearity and many design parameters for tailoring the fiber's dispersion characteristics, i.e., spacing, size and geometry of the hole structure, particularly attractive for efficient frequency conversion. First applications exploited the spectral broadening in PCFs for multiplex CARS, i.e., spectral imaging. Supercontinua (SC) from PCFs enable the acquisition of CARS spectra and spectral images covering 800 to 4000 cm^{-1}.[76, 82-87] However, without a spectral detection the spectral resolution and thus contrast of SC based sources is poor, unless imaging strategies like spectral focusing are used (see section 4.6.4).

SSFS as another mechanism for frequency conversion in optical fibers has several advantages in comparison to SC. First, the output is more stable resulting in a defined spectral and temporal pulse shape. Second, the conversion efficiency of the pump pulse to the redshifted soliton pulse is significantly higher. Conversion efficiencies of 80% have been reported, but the conversion efficiency is decreasing for longer wavelength generation.[78] Third, the soliton spectrum is not as broad as an SC spectrum, hence the spectral energy density is significantly higher due to the lower spectral width. While spectral tuning is not possible and not needed in case of SC, spectral tuning of the soliton output can be realized by varying the input power, e.g., from 1000-3000 cm^{-1}. However, the spectral width of the soliton is on the order of several 100 cm^{-1} and therefore exceeding the Raman line width. This results in poor spectral resolution when combining a 160 cm^{-1} Ti:Sa-pulse and 90 cm^{-1} spectral width soliton from a PCF for CARS imaging.[88] When using spectral focusing of a 27 fs Ti:Sa laser and a 45 fs soliton generated in a PCF, tuning across the bandwidth of the pulses of 400 cm^{-1} has been achieved at 8 cm^{-1} spectral resolution, while the system enables to access the spectral range of 500-3000 cm^{-1}.[89] Alternatively the spectral resolution can be improved by either using a spectrograph or subsequent spectral compression of the soliton as will be discussed later.[78]

In contrast to SC and SSFS, four wave mixing (FWM) allows generating spectrally narrow emission similar to parametric conversion employed in periodically poled lithium niobate (PPLN) crystals in an OPO. Hence, substituting the PPLN in an OPO by a PCF results in a fiber-OPO (FOPO).[90] Since the spectral separation between the pump laser and the generated signal and idler can be much smaller than in conventional OPOs, a larger part of the Raman spectrum can

be covered by such a source without the need for a second OPO for imaging resonances below 700 cm^{-1}.[71, 73, 75]

Before presenting all-fiber based light sources for CRS, another compact alternative will be briefly introduced.

3.1.5 Microchip-fiber laser

Microchip lasers potentially enable to realize ultracompact lasers for CRS imaging. In contrast to the aforementioned lasers, microchip lasers emit ns pulses at lower repetition rate. In 2008 CARS imaging using a Q-switched Nd:YAG microchip laser operating at 1064 nm has been demonstrated. The laser emits 8 µJ pulses at 6.6 kHz repetition rate with <1 cm^{-1} spectral resolution and <1 ns pulse duration. A part of the laser is used as pump laser, another fraction is used for frequency conversion in a PCF generating broad band emission covering 2000 cm^{-1}, which is used as Stokes beam.[91] While imaging of single cells by multiplex CARS has been demonstrated, the imaging speed has been limited by the low repetition rate of the laser to 300 ms. However, recently 30 ms per pixel have been realized using a 27 kHz laser.[92] While microchip lasers are very compact, they are not suited for fast biomedical imaging application. Alternatively, fiber lasers combine a small footprint with high peak power and repetition rate for fast imaging application. The current developments in this field are summarized in the following section.

3.1.6 Fiber laser for CRS

When compact and robust light sources are needed, fiber laser technology is most promising. Due to the large surface to volume ratio, fiber lasers are thermally very robust and insensitive to temperature changes or humidity. Fiber lasers provide extraordinary gain and an excellent spatial beam profile. In order to realize an all-fiber laser source for CRS imaging, there are two strategies: (i) synchronizing two fiber lasers or (ii) using a fiber laser to pump a passive fiber utilizing fiber based frequency conversion processes for generating a synchronized emission at a spectrally separate wavelength.

For the first case there are only a limited number of active fibers available, doped with Yb, Er or Tm. Hence, by synchronizing these lasers, only a part of the Raman spectrum can be covered. Yb fiber lasers are tunable from 1000-1100 nm, whereas the tuning range of Er is in the range from 1500-1600 nm and Tm can be tuned from 1800-2100 nm. Hence, only the combination of Yb and Er fiber lasers allows accessing the C-H-stretching vibrations directly. An all-fiber laser source combining synchronized Yb and Er-fiber-oscillators has been used for CARS imaging.[93] However, for technical reasons excitations wavelengths in the NIR are disadvantageous, since sensitive detectors as CCDs or PMTs available for the VIS do not exist for the NIR. Furthermore, well corrected NIR-microscope optics are also not available for the NIR. Here nonlinear frequency conversion processes in optical fibers allow generating light in a much broader wavelength range than active fibers. These fiber based frequency conversion processes are supercontinuum (SC) generation, soliton self-frequency shift (SSFS) and four wave mixing (FWM). SC is a combination of nonlinear processes like self-phase modulation, FWM and SSFS leading to a huge spectral broadening of the initial pulse at the cost of low spectral power and higher noise. Hence, SC is primarily used to generate a broadband Stokes pulse for detection of the CARS spectrum.[76, 82-86, 94, 95] SSFS has been used to generate a synchronized output at longer wavelengths for CARS imaging in the CH-stretching spectral region.[96] 60 fs pulses of an Erbium doped Raman shifted fs fiber laser are used to pump an ultra-high nonlinear fiber (UHNLF) at 810 nm generating solitons at 1053 nm, which corresponds to 2850 cm^{-1}. Spectral tuning from 1000 to 1100 nm is realized by adjusting the input power such that the tuning range of 2500-3200 cm^{-1} covers the CH-stretching Raman resonances. Since the soliton generation is closely related to material constants of the optical fiber, the soliton is spectrally as broad as 80 cm^{-1}. Also the total power is limited to 1.5 mW. By employing spectral focusing, the spectral resolution can be increased at the cost of lowering the peak intensity.[97] By adding second order dispersion using a grating pair, the pulse durations of a 1036 nm 185 fs pump pulse and of a 70 fs Stokes pulse generated by SSFS in a photonic crystal fiber (PCF) are increased to 1.9 and 3.8 ps, respectively, enabling CARS and SRS imaging of polystyrene beads at 1000 cm^{-1} with 15 cm^{-1} spectral resolution.[98]

In order to improve the spectral resolution, subsequent spectral compression by SHG can be employed.[99] The output of an Er-laser is split and amplified in two Er-amplifiers. One output is directly frequency doubled by SHG and used as pump-laser for CARS imaging at 775 nm, the other output is frequency shifted by SSFS in a UHNLF. A specially designed periodically poled Lithium-Niobate crystal (PPLN) is used for frequency doubling a spectral fraction of the UHNLF-emission. Tuning is realized by adjusting the PPLN from 850 to 1100 nm, which corresponds to 1100 – 3800 cm^{-1}. The output power of the tunable Stokes varies across the tuning range from 5 to 20 mW.[99, 100]

Hence, while SC and SSFS enable spectral tuning, both the output power and the spectral resolution are lower in comparison to solid state lasers. However, there is a fiber based mechanism for frequency conversion, which enables the generation of intense, spectrally narrow and tunable laser radiation: degenerate four-wave mixing (FWM).[101] Here, an intense pump pulse generates in a specially designed photonic crystal fiber a shorter wavelength signal and a longer wavelength idler by FWM. The dispersion of the PCF determines the spectral separation of signal, pump and idler, which can be tailored by the geometry of the fiber. The complete Raman spectrum is accessible; and spectral tuning can be realized. Tuning of signal and idler wavelength is accomplished by changing the pump laser wavelength. Furthermore, the three spectral components of the residual pump laser and FWM signal and idler offer three different combinations for CRS: signal-pump, and idler-pump for CSR imaging at different excitation wavelength, and signal-idler for imaging high wavenumber Raman resonances. Since all three wavelengths are emitted from a single fiber end, they are perfectly aligned, significantly reducing the need for adjustment. Even an all-fiber setup is possible.[102] However, signal and idler pulses are on the order of 30 cm^{-1}, thus; spectrally broader than the pump beam, since the FWM

generation starts from quantum noise.[101] While the spectral resolution of 30 cm^{-1} limits the image contrast, it is possible to reduce the spectral width towards the transform limit by two strategies: using an external seed laser or a feedback cavity.

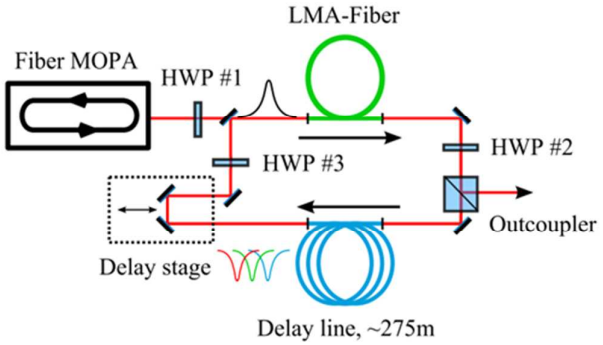

Figure 3: Experimental setup of a FOPO based on FWM for high spectral resolution CARS imaging.[103] (Reprinted with permission from T. Gottschall, T. Meyer, M. Baumgartl, B. Dietzek, J. Popp, J. Limpert and A. Tünnermann, Optics Express, 2014, 22, 21921-21928. Copyright 2014 Optical Society of America.)

First, the FWM process can be seeded by a spectrally narrow external seed laser within the spectral window of signal or idler for FWM generation. In order to circumvent the problem of synchronization, a cw laser source can be used, since mW of cw power suffices. By applying this concept using 1.6 W from a 54 MHz Yb fiber laser with 7.7 ps pulse duration in combination with a tunable diode laser, 166 mW of signal at 1.8 ps duration and 1 nm spectral width (18.5 cm^{-1}) have been realized.[80] In this work, the laser was tunable across the C-H-stretching region from 2650 to 2950 cm^{-1} by changing the wavelength of the Yb pump and the seed laser at an overall conversion efficiency of 10%. In order to realize even higher spectral resolution, longer pulse durations have to be used. Using a Ti:Sa-laser for seeding the FWM signal generated from a 140 ps Yb pump laser, 33 mW of signal power at 0.8 cm^{-1} spectral resolution have been achieved for 65 ps signal pulse duration, which is close to the transform limit of 0.5 cm^{-1}. Due to the broad tuning range of the Ti:Sa seed the laser is tunable across the complete Raman spectrum.[101]

Alternatively, self seeding with a spectrally narrow portion of either the generated signal or idler emission can be used to decrease the spectral width of the FWM emission. This is beneficial, since there is no need for a second tunable laser source, such that the tuning range is not limited by the seed laser. Furthermore, the conversion efficiency is higher and the relative intensity noise (RIN) reduced with respect to the OPA, which is crucial for SRS imaging.[81] By fiber integration of the FOPO, also a more compact and robust laser source can be realized.[81, 103] When using a 46 MHz Yb laser, 140 mW signal at 8 cm^{-1} spectral resolution has been generated using 850 mW of pump power corresponding to 13-20% conversion efficiency within the tuning range from 2740-3150 cm^{-1}. While the output power can be increased further to 200 mW, this results in an increase of the laser noise. Furthermore, for stable operation filtering of the idler feedback is required.[81] Using a laser with 750 kHz repetition rate of 40 ps pulses an even higher conversion efficiency of 38 % has been demonstrated.[103] 180 mW of signal power at 1 cm^{-1} spectral resolution has been generated. The system is depicted in figure 3.

Hence, FOPOs based on degenerate FWM are very promising light sources even in comparison to conventional state of the art OPOs ideally suited for biomedical application: the FWM emission can cover the complete Raman spectrum at a spectral resolution, repetition rate and peak power, which is at least comparable to solid state lasers and OPOs. Furthermore, signal and idler wavelengths close to the pump wavelength can be generated, while OPOs using PPLNs cannot generate light close to the pump wavelength. Finally, the sources can be fully fiber integrated in the near future, resulting in a very compact and maintenance-free laser.

3.1.7 Continuous wave (cw) laser configurations for CRS

A significant complication of CRS microscopy is due to the need to synchronize two lasers. However, if a pulsed laser is combined with a cw laser source, there is no need for synchronization, rendering this approach particularly simple and robust. In a spectroscopic application, a broadband few cycle Ti:Sa-laser was used to illuminate the sample, while a 532 nm cw laser was used to detect spontaneous and coherent Raman signals.[104] The overall CARS signal yield was 2% of the total signal. To increase the efficiency of CARS signal generation, higher repetition rate lasers can be used. However, when the pulsed laser is not illuminating the sample, no CRS signal will be generated, resulting in either relatively high light levels on the sample or low signal yield.

An even simpler approach is using two cw lasers directly. While the nonlinear signals are weaker when using cw illumination with low peak power, SRS imaging has been successfully demonstrated, since SRS depends only on the square of the excitation power. Since the SRS signal is detected by a modulation transfer mechanism, cw lasers offer the advantage of potentially being much more stable, i.e., less noisy, allowing much smaller modulations to be detected. As a proof of principle, air bubbles immersed in the organic solvent dimethylsufoxid (DMSO) were imaged by SRS by combining the SHG of Nd:YVO4 at 532 nm as pump laser with a 633 nm HeNe-Laser as Stokes to image the spatial distribution of the 3000 cm^{-1} Raman band of DMSO utilizing 4 kHz modulation of the pump beam by a chopper and 100 ms integration time per pixel. While this proof of concept experiment is too slow and not sufficiently sensitive for fast imaging application, further improvements are possible.[105]

By combining a tunable cw diode laser emitting at 765-781 nm with a Stokes laser at 982 nm, SRS imaging from 2620 to 2880 cm^{-1} has been realized. In order to remove electronic background signals, a dual modulation scheme has been employed. As expected, the signal level of cw SRS is 1300 times smaller as compared to 80 MHz lasers and 5 ps pulse duration of similar average power. Nevertheless, liver tissue has been imaged using 1 ms pixel dwell time, which is still significantly slower compared to pulsed lasers offering video rate image acquisition.[106]

To overcome this problem, the cw laser can be electronically modulated. This so-called time-lens approach allows generating a synchronized pulse train. In a first realization, a cw laser operating at 1064 nm was synchronized to a 76 MHz Ti:Sa-laser of 2 ps pulse duration generating 240 mW of output power and 1.7 ps pulse duration with only 50 fs timing jitter. While synchronization across 0.8 ns is achieved using electronic delays, two Yb amplifiers and dispersion compensators are needed to generate transform limited powerful pulses.[107] This concept is improved, when additionally modulating the current of the laser diode directly at lower frequency of 2.29 MHz for Lock-In SRS detection, resulting in an improved extinction ratio and higher output power up to 400 mW. Detection of 28mM DMSO has been demonstrated.[108]

An exciting concept based on NIR cw lasers enabling fast spectral imaging is described in the following.

3.1.8 Highlight – Time encoded Raman imaging

The detection of a large fraction of the Raman spectrum using simple all-fiber laser sources has been recently demonstrated utilizing time encoded Raman imaging (TICO). Here fast wavelength sweep cw probe lasers are used providing a spectral coverage of 750–3150 cm^{-1} at 0.5 cm^{-1} spectral resolution. 32 point spectra were recorded in 636 µs, hence only 19 µs per spectral point. In order to improve the generation of the SRS signal, the cw lasers were modulated resulting in ns-excitation pulses. In principle, transform limited spectral resolution below 0.01 cm^{-1} can be achieved. SRS imaging of lignin and olive oil at 2.5 µs per spectral position and 157 µs per spectrum in the range of 1675-1575 cm^{-1} has been demonstrated, while the acquisition of high quality Raman spectra is possible within 250 µs per spectral point [109].

While CRS requires sophisticated light sources for efficient signal generation, the demands on the microscope and detectors vary according to the method, which will be presented in the following.

3.2 Laser scanning microscopes

Depending on the specific method of CRS the details of microscope and detectors can vary significantly, as illustrated in figure 4 for SRS, CARS or RIKE. Additionally there are major differences according to the imaging strategy with respect of the acquisition method for single Raman-band CRS images and for hyperspectral CRS images. In this section we will focus on the equipment for single Raman band CRS imaging using a collinear illumination scheme by laser scanning the sample and the acquisition of hyperspectral data by sequential image acquisition at different Raman resonances.

Due to the coherent nature of the CRS signals and the higher signal yield in comparison to spontaneous Raman, laser scanning microscopes (LSM) are routinely employed enabling fast imaging by coherent Raman microscopy for selected Raman resonances. CRS images can be acquired as fast as with video rate image acquisition, which corresponds to pixel dwell times of ~100 ns per pixel and total exposure times of fractions of seconds per image.[25, 26, 38, 110] For the acquisition of complete spectra by multiplex-CRS, longer integration times are needed, such that often stage scanning is employed.

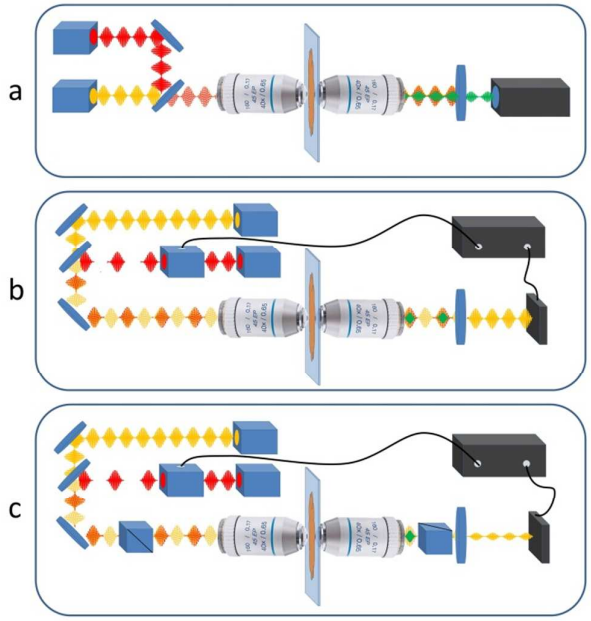

Figure 4: Scheme of CARS (a), SRS (b) and RIKE (c) microscopy experiments. For CARS experiments two synchronized lasers and an appropriate short pass filter are needed, rendering CARS the simplest implementation of CRS. SRS requires in addition an optical modulator and a lock-in detector, while for optical heterodyne RIKE additional polarizers are needed.

For CRS imaging, any commercial laser scanning microscope can be used in combination with a suitable light source presented in the preceding section. Since often NIR lasers are employed, multiphoton laser scanning microscopes offer the best optics for chromatic correction and high throughput of the NIR laser beams. However, there are a few differences in contrast to LSMs used for multiphoton fluorescence. First, CRS microscopes are equipped with large area non descanned detectors in forward direction, since the CRS signals are predominantly emitted in the propagation direction of the laser. This is due to the fact, that the laser itself is detected in case of RIKE and SRS, while due to the phase matching condition the CARS signal is most efficiently generated in forward direction. Second, high numerical aperture (NA) condensers provide the highest collection efficiency and minimize image artifacts in SRS by photothermal and position dependent interference effects. The key element for CRS imaging using an LSM is the illumination optics consisting of scan and tube lens and the microscope objective. The scan and tube lens are used to image the steered laser beams on the galvanometric mirror surface onto the back focal plane of the microscope objective. The microscope objective focuses the laser beams to a diffraction limited spot in the specimen. In contrast to multiphoton imaging methods utilizing a single NIR laser, the need for two synchronized lasers results in much tighter specifications on the chromatic aberrations of these optical elements, since any longitudinal or lateral chromatic

aberration reduces the overlap of the focal spots of pump and Stokes laser, which results in a significant reduction of the CRS signal. The best performance is possibly offered by systems specifically designed for CRS microscopy.[111, 112] However, there is currently no microscope equipment for biomedical applications available, which operates further in the NIR than 1100 nm.

For live cell and tissue imaging high NA water immersion objectives are routinely used offering high spatial resolution and collection efficiency of the CRS signals in backward direction. The best chromatic correction provide to date special NIR objectives, which are designed for multiphoton application, offering high NIR transmission.[113, 114] However, due to different concepts in the optical design it is usually not possible and not recommended to combine objectives and microscope platforms of different manufacturers. This is due to the fact, that first the tube length and thus the focal length of the tube lens is different for the major manufacturers. Second and even more important, the chromatic aberrations are corrected differently, which is why combining optics from different manufacturers can result in over or under-correction of chromatic aberrations in the specimen plane, which is usually not tolerable for CRS microscopy.

In order to improve the performance of the microscope when using wavelengths beyond the color correction range of the objective and microscope, separate telescopes in pump and Stokes beam path can be used to adjust the divergence of both beams in order to focus them to the same focal plane. [25, 115, 116] However, this adjustment is wavelength dependent and complex.

Since pulsed excitation lasers used for CRS provide peak intensities and wavelengths employed for multiphoton microscopy, the LSMs can be equipped with beam splitters and filters to simultaneously register other multiphoton modalities such as second and third harmonic generation (SHG, THG) and two or three photon excited fluorescence (TPEF, 3PEF).[117]

While there is no big difference in the common LSM layout, the detectors for RIKE and SRS are completely different in comparison to CARS and multiphoton fluorescence. The different detectors for CRS imaging will be presented in the following section.

3.3 Detectors

3.3.1 Single channel detectors

Depending on the specific technique, different detectors are used for CRS microscopy, which is due to the different signal strengths. While CARS relies on the detection of few photons generated at the anti-Stokes frequency, heterodyne RIKE and SRS require the detection of a small modulation transfer of only 10^{-4}…10^{-6} from one onto the other laser after passing the sample. Here a large dynamic range of the detector is essential in order to precisely detect all photons in the laser beam.

Thus, for CARS sensitive detectors like photomultiplier tubes (PMT) or avalanche photodiodes are employed.[68] PMTs combine high gain of up to 10^8, a fast response in the range of ns and a large active area up to several cm² for non-descanned detection with quantum efficiencies up to 40%, which is almost comparable to CCDs. Due to the longer excitation wavelengths in the NIR, often NIR enhanced PMT detectors are used. But PMTs are only sensitive to wavelengths up to 920 nm.[118] Hence, the limited spectral response is a major reason why NIR lasers far in the NIR cannot be used for CARS microscopy. Here, avalanche photodiodes (APD) provide additional spectral response up to 1150 nm and peak quantum efficiencies of 85%, but the active area is max 1 cm² and the gain is lower in comparison to PMTs. While APDs are fast, the large area versions are slower than PMTs with response times of ~45 ns, which is not sufficient to temporally resolve pulses from an 80 MHz pulse train. However, they can be used in photon counting mode for the detection of sparse photons.[119]

For SRS and RIKE PMTs or APDs are not suited due to their low saturation light levels. Here diodes are employed, which enable the detection of high power laser beams without attenuation. In this case, the highest signal to noise ratio can be achieved. To maximize the saturation current, large area photodiodes are used with 1 cm² active area, which enable detecting ~50mW of laser light, when the whole area is evenly illuminated. However, in order to detect the small modulation induced by SRS or RIKE, a sensitive lock-in amplifier has to be used.[28, 120] Standard instruments usually do not permit fast imaging due to minimum time constants of 20 µs[28] or 0,8 µs,[120] which is why for video rate SRS custom design lock-in amplifiers are used.[26, 121] However, there are other detection methods in order to improve the detection of SRS and RIKE signals. One such technique is balanced detection.[32, 121, 122] Here, the laser is split. One part is passing the sample and the other fraction is not. Both beams are then detected by two parallel photodiodes allowing to remove relative intensity noise of the laser, which is particularly important for fiber lasers, which are noisier than solid state lasers.[31, 32] Alternatively, also a collinear illumination scheme can be used, in which the laser is split in two and one fraction delayed in time by almost the pulse separation, which enables cancelling the RIN noise of the laser when Fourier-transforming the signal.[121] Another approach is using tuned amplifiers.[123] In contrast to a Lock-In amplifier, which serves as an electronic bandpass filter for the detector signal at the modulation frequency, the tuned amplifier is a resonant circuit at the readout of the photodiode, which strongly amplifies signals of the modulation frequency by orders of magnitude. The system achieves similar performance as a Lock-In, but is much smaller. Hence, tuned amplifiers offer a strategy for multiplex SRS. In the following section we will introduce detectors for spectrally broadband CRS.

3.3.2 Multichannel detectors

The simultaneous detection of a broad spectral range by CRS can be realized most effectively for CARS, while the need for a Lock-In amplifier complicates the multiplex-SRS and RIKE detection, since multichannel Lock-In amplifiers are not widely used and complex devices. A few concepts are limited to slow scanning due to modulation frequencies below 100 kHz.[124] Recently, multiplex SRS has been realized using a 16 channel diode array. Tuned amplifiers are integrated in the read-out

circuit of the diode array enabling the simultaneous detection of 16 spectral channels.[39] In principle, SRS can be also detected without Lock-In by subtracting accumulated signals when the modulated beam is off from signals, when the beam is on. This enables the measurement of SRS spectra within 20 ms using a fast CMOS array using 54200 individual frames.[125] But the need for fast and extensive data processing in order to extract the small fluctuations caused by SRS is currently not competitive with other approaches. Especially since the data transfer of 10^5 frames takes another 5 minutes, thus, much longer than data acquisition of only 20 ms acquisition and 20 ms per spectrum is not faster than advanced realizations of multiplex CARS.

Multiplex CARS is therefore the most widely used modality for the simultaneous detection of signals from multiple Raman resonances, requiring detectors known from spontaneous Raman spectroscopy. The major difference is the collection of CARS signals in forward direction, Using a fast electron multiplying charged coupled device (EMCCD) enables the detection of CARS spectra of biological samples covering 470 to 3800 cm^{-1} at less than 13 cm^{-1} spectral resolution within 3.5 ms pixel dwell time.[40]

4. Raman signal acquisition strategies

Raman microspectroscopy has become a versatile tool in biomedical research covering a wide range of applications on the small scale, such as the identification of single prokaryotic cells and eukaryotic cells, analysis of mechanical stress in cells, cell sorting, investigation of cellular compartments and intracellular changes, but also on larger scale, such as tissue histopathology, and *in vivo* cancer detection. Due to this great variety of applications many different Raman signal acquisition strategies have been developed. Confocal Raman spectroscopy, Laser-Tweezers Raman spectroscopy (LTRS), point-scanning Raman microscopy, line-scanning Raman microscopy, wide-field illumination, and multi-foci illumination, are all common approaches to acquire Raman signal of biological samples. The right choice of acquisition modality is key to generate strongest Raman signals, to maximize background suppression, and to produce interpretable and reproducible data. In this part we will review different acquisition modalities for Raman spectroscopy and will include suggestion for possible applications.

4.1 Confocal Raman microspectroscopy

In the most elementary implementation of Raman spectroscopy a monochromatic Gaussian excitation beam is focused by an objective lens into the sample plane, generating a Raman signal from the specimen. The signal is collected by the same objective lens, and after passing some optical elements imaged onto the entrance slit of a spectrometer. After passing a dispersive element the signal is collected by a detector.[126] This was the standard configuration of Raman spectroscopy for a long time, and was sufficient for the analysis of bulk samples. In bulk samples molecular compounds are homogenously distributed in a volume much larger than the focal volume, and typically at high concentrations, so that background contributions from sample medium and substrate do not obscure the Raman signal.[127-129] In biological samples, however, the molecules are present at low concentrations and are heterogeneously distributed at macroscopic sampling volumes. Moreover, background contributions and sample autofluorescence inherent from the sample or from exogenous molecules can easily overwhelm the weak Raman signals. A confocal approach that allows optical sectioning of the sample and reduces out of focus contributions came as an obvious solution to this problem. When an objective lens focuses the excitation light to a diffraction-limited volume a Raman signal is generated not only in the focal volume, but also anywhere along the path of the excitation light, which includes the sample embedding media, the sample substrate, and even the optical elements, contributing to the total detected signal. While, in bulk sample the amount of Raman signal from the sample is typically much larger than the background contributions, for tiny sample volumes, such as single cells, the out-of-focus contributions can easily overwhelm the Raman signal from the focal volume. Figure 5 shows a schematic drawing of such a confocal arrangement.

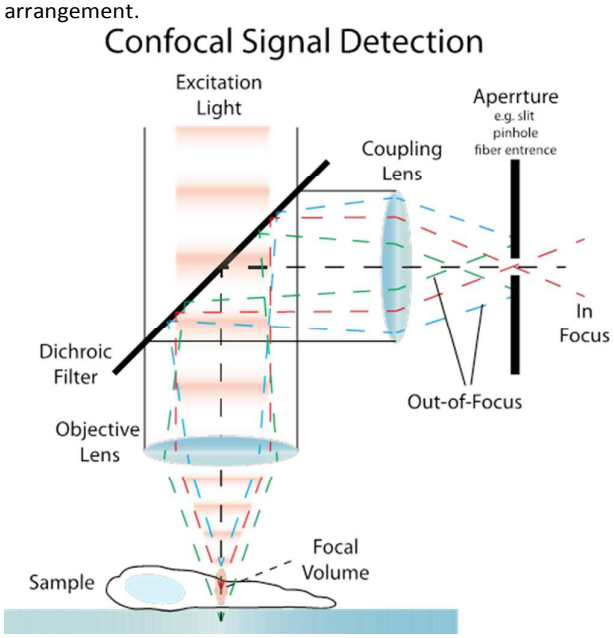

Figure 5: Schematic of confocal signal detection. The excitation light is focused to the sample plane. The generated Raman signal is collected by the same objective lens and separated from the excitation light by a dichroic beam splitter, and imaged onto the aperture. The in-focus generated signal, in red, can freely pass the aperture. Signal generated below the focus, in green, and signal generated above the focus, in blue, are rejected by the aperture.

An infinity corrected objective lens focuses the excitation light into the sample plane. A signal is generated in the focal volume, but also above or below the focal volume. The objective lens collects the all signal contributions, and after being separated from the excitation source imaged into the

conjugated image plane, where an aperture is located. Usually this aperture is a pinhole, but also a slit or multimode fiber is possible. Only beams that are originated in the focal volume can pass the aperture, all other contributions are rejected.

While the first confocal scanning microscope was described and patented by *Minsky* in 1957,[130] the first commercial implementation of a confocal laser-scanning microscope, according to *Inouè and Pawley*[131], was reported not until 1987. It does not come as a surprise that after the great success of confocal laser-scanning microscopy in biology, a translation of this approach to Raman spectroscopy would prove beneficial. In a key publication *Puppels et al.* in 1990 have shown that the implementation of confocal Raman microspectroscopy allowed them to acquire Raman spectra of cytoplasmic and nuclear regions of eosinophilic granulocytes and chromatid of metacentric Chinese hamster lung cell metaphase chromosome.[132] This publication started a paradigm change for Raman microspectroscopy of biological samples, underlining that it is indeed possible to acquire label-free information from diffraction-limited volumes of single cells. It is important to note that confocality in Raman microspectroscopy has already been used before that, e.g. *Abraham et al.*,[6] but the degree of confocality was much worse than present in the paper by *Puppels* and colleagues. In a follow-up publication the researchers characterized in depth different confocal parameters of their Raman microscope, achieving a lateral resolution of 0.45 ± 0.05 µm and an axial resolution of 1.3 ± 0.1 µm.[133] *Tabaksblat et al.* described a simple theoretical model for a confocal signal detection and showed that the experimental results of confocal Raman signal detection of thin polymer films follows their theoretical model.[134] Besides showing that polymer films could be resolved in depth along the optical axis with a resolution of 3 µm, the researchers were also able to show that the fluorescence signal could effectively be suppressed by a factor of 10 using a confocal setup. *De Grauw et al.* used Gaussian beam theory introduced by *Wilson* [135] to describe the axial resolution of a confocal Raman setup and compared it to experimental results.[136] The approximation was determined 'for samples larger than the beam diameter and thicker than the confocal parameter of high numerical aperture objectives', which applies to a majority of biological samples such as eukaryotic cells, tissue sections and others. It was shown that the simplified Gaussian model to theoretically describe confocality is in excellent agreement with the experimental data for circular and slit apertures.

While the principles of confocal Raman spectroscopy and microscopy are very well defined, the practical implementation according to *Everall*,[137] is frequently not at pair with reality. *Everall* has identified some key issues that can lead to misinterpretation of the depth information in confocal Raman spectroscopy. One of the major problems occurs from spherical aberrations when using metallurgic objective lenses. These objective lenses are specifically designed to image opaque surfaces, not transparent materials. Though, not mentioned in the publication, this can specifically apply to unstained histopathological tissue slides which are investigated with air objective lenses. The spherical aberrations occur because of a mismatch between air and sample interface. When a depth profile is acquired the excitation light is focused much deeper into the sample. Hence, the mechanical translation of objective or sample along the z-axis when focusing into the specimen does not correspond to the shift of the focus position. It is larger than the reduction of the sample-objective distance. This can delude to believe that the sample is thinner than it actually is.[138] In optical microscopy it is widely known that spherical aberrations can be greatly reduced by matching the refractive index of the immersion media of the objective lens with the refractive index of the sample. This reduces the phase mismatch between the sample and the objective lens and can be achieved by using an oil-immersion or water immersion objective lens.

Nowadays, Raman microspectroscopy of biological samples, such as single prokaryotic and eukaryotic cells, or cellular compartments can rarely be found in a not-confocal configuration. It is important to emphasize that confocality is a very precisely defined property, and the implemented aperture should be the size of the conjugated image of the focal spot. Confocality of a system is bound to the magnification of the focal spot; hence, when the objective lens is changed to a different magnification it has to be accompanied by a change in the size of the aperture, and vice-versa. Frequently it can be seen that people are more interested in having a large signal rather than high confocality, and optimize the system for that, forgetting that with this confocal properties are reduced and out-of-focus background contributions are increased.

4.2 Laser-Tweezers Raman spectroscopy (LTRS)

Manipulation of micro-sized particles using optical pressure forces has been first reported by *Ashkin* in 1969, and rapidly gained broad popularity in physical and biological sciences.[139] When light passes under tight focusing conditions – such as in microscopes with high numerical aperture objectives – from a medium with a low refractive index into a particle with a high refractive index the particle experiences a radiation force due to the change of momentum of the photons; this also occurs when the photons exit the particle. When a linear light gradient is applied across a dielectric particle, as depicted in figure 6a, the net force F_{net}, resulting from the change in momentum of photons acting on the particles will point in the direction of highest optical intensity. This is because the number density of photons is highest; as a result the total momentum change will be greatest. This gradient force, which acts on the particle, will move it along the gradient. In case of a Gaussian illumination profile that is typical used in optical microscopy the highest intensity is in the center of the illumination beam, radially decreasing. By applying the same consideration it can see that the forces acting on the particle equalizing each other, resulting in a net force F_{net} that keeps the particle stable and central inside the beam acting as an optical trap, figure. 6b. Optical tweezers have found a wide

range of applications in biomedical research, because they uniquely allow force measurements on the order of pN, something that was previously not possible.[140-142] Especially, the investigation of molecular motor proteins, such as myosin, kinesin, dynein, and forces, which are exhibited in ribosomal RNA translation, have benefited from this approach, see review *Capitanio and Pavone*.[143]

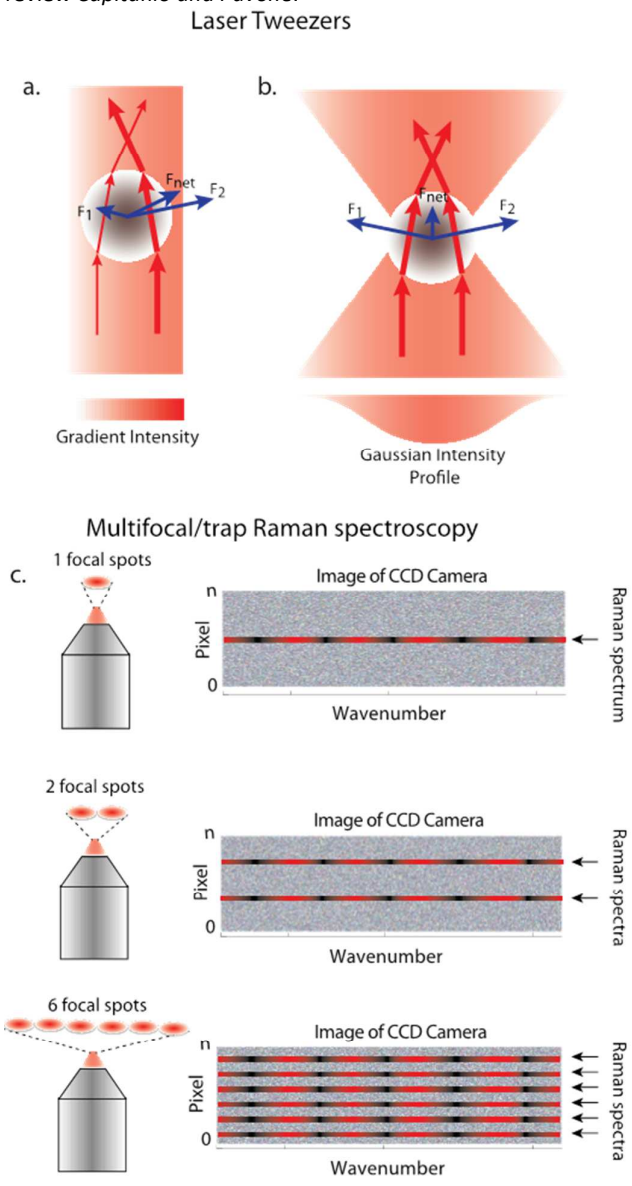

Figure 6: A linear intensity gradient is applied across a dielectric particle. The light is diffracted when it enters the particle, and when it exits the particle. Because the momentum of the light is conserved the particle is experiencing a force. The change in the momentum is higher for higher intensities, resulting in a gradient force (A). A Gaussian illumination profile is used. The net resulting force F_{net}, keeps the particle stable in the center of the beam. When a Raman signal is generated from one focal volume it is imaged into one horizontal line on the CCD detector (B). When two or more focal spots are generated the signal for each spot is imaged into separated vertically displaced locations on the CCD detector (C).

In the simplest arrangement LTRS is used to probe one cell at a time, resulting in low throughput, and making it unsuitable for many biomedical applications. One possible approach to increase the throughput in LTRS is by multiplexing the number of traps created in the sample plane. Each focal spot is subsequently imaged on different vertical positions of the CCD detector and the spectral information from each trap can be acquired simultaneously, see figure 6c. A multiplexing approach for cell manipulation without Raman spectroscopy has already been shown by *Misawa et al.* in the early 90's.[144]

The first implementation of a dual-trap for Raman spectroscopy was done by *Q. Li et al.*, by splitting a beam with a conventional 50/50 beam-splitter, and recombining them at a slight angular separation.[145] The setup was used to investigate budding yeast cells and *Bacillus* spores over an extended period of time. One of the major disadvantages with this approach is that both traps are steered by the same pair of galvo-scanning mirrors, making the trap inflexible for sophisticated manipulations. This approach was quickly superseded by a new implementation from the same group, where the laser beam is rapidly scanned over the particles located in the sample plane. [146] Instead of creating multiple traps through beam-splitting the system uses a time-sharing of optical traps. The beam moves so rapidly over the particles they are trapped in a fixed position without being constantly exposed to the excitation. Up to 10 cells could be captured with this approach. The signal from each trap is than vertically displaced on a CCD detector using an additional galvo-scanning mirror. Almost simultaneously *Rui et al.* developed an identical approach of time-sharing optical traps, and used it for the investigation of RBCs.[145]

There are two major limitations of the time-sharing approaches: the number of particles that can be trapped is limited; the CCD detector that detects the traps has only a finite horizontal dimension, so that for a high number of particles an overlap between the spectra will become unavoidable. *Kong and Chan* solved these problems by first using a spatial-light modulator and creating a large number of steerable traps, and instead of imaging the spectra on the CCD detector only in the vertical dimension, the spectra were also imaged in the horizontal dimension on the CCD detector.[147] The overlapping spectra were retrieved with high fidelity using a mathematical approach. Currently, up to 20 traps can be evaluated simultaneously, with prospects of more than 100.

A detailed review on LTRS can be found elsewhere [148, 149]. A very detailed protocol on the implementation of a LTRS setup combined with fluorescence and phase-contrast microscopy was written by *Kong et al.* [150]

4.3 Point-scan and Multi-focal Raman Imaging

In many biomedical applications single-point spectra provide sufficient information to properly characterize samples. In many applications, however, especially when dealing with highly heterogeneous samples, such as single cells or histopathological tissue sections this approach does not always suffice, and can provide imprecise or erratic information. For

example, cellular changes that occur in the nucleus can be quite different to changes that occur in the cellular periphery and could be missed by a single-point measurement. Therefore, the application of Raman spectroscopy in imaging mode is of great importance to properly characterize the sample.

The first Raman imaging microscope was proposed and implemented by *Delhaye and Dhamelincourt* in 1974.[151] In this path-setting contribution the researchers developed and compared three different implementations for Raman mapping. The first approach utilizes the scanning of a diffraction-limited spot across the sample; a point detector detects a single vibrational band, and the image of the sample is reconstructed. The second approach rapidly scans a spot along a line; the generated signal from that line is detected at once on a multichannel detector. The third approach uses a wide-field illumination of the sample; the signal of a selected Raman vibration is imaged on a multichannel detector. Until today, each of the suggested acquisition methods is still in use as suggested, or with a few modifications.

The simplest implementation for Raman mapping, which is also most commonly used, is the raster-scanning of the focal spot over the sample, creating a hyperspectral data set from any position. Typically the objective lens remains stationary, whereas the sample is located on a motorized translational x-y stage, which is raster-scanned across the focal spot with a predefined point dwell-time, see figure 7 (left). The Raman signal for every point position is individually detected. A great advantage of this approach is, besides providing diffraction-limited optical resolution, the common implementation in a confocal geometry. This allows the acquisition of 3-dimensional images with full vibrational information from any recorded point of the sample plane. According to the Nyquist theorem the step size in point scanning mode should be two or three times smaller than the laser spot size to give optimum lateral resolution. Decreasing the step size from 1 µm to 0.5 µm or 0.33 µm increases the number of spectra in a 2-dimensional image by a factor 4 or 9, respectively. Due to the typically small Raman scattering cross-section and the resulting low signal yield, the total exposure time to collect Raman images in this acquisition mode is relatively long which is not compatible with high throughput and time-resolved imaging applications of biological samples. One possible modification to improve the signal acquisition is, similar as in LTRS, by using multifocal acquisition. *Okuno and Hamaguchi*, developed a multifocal imaging approach by creating multiple beamlets, using a micro-lens array.[152] After passing an 8 x 8 pinhole mask the beamlets are imaged into the sample plane. The generated signal is imaged onto a rectangular arranged 8 x 8 fiber bundle that is rearranged into a line on the other side and attached to a spectrometer. Each focal spot is than imaged to a different horizontal location on the CCD camera, akin to multi-focal trapping. This allows the acquisition of 48 spectra simultaneously, and improves the data acquisition by the same number. *Kong et al.* implemented a scanning approach with galvo-mirrors where a beam Gaussian beam is scanned over the sample plane, and the generated Raman signal is projected onto different position of the CCD detector using a third galvo-mirror.[150]

The researchers suggest that this approach results in a 40 times signal speed improvement, while maintaining high confocality. In a follow-up publication the researchers were able to achieve a parallel acquisition from 80 different locations in the sample plane. [153] An implementation of multifocal Raman imaging generated by a spatial light modulator (SLM) was implemented by Qi and Shih.[154] The setup allowed acquiring spectra from up to 30 particles in parallel, and can be used for Raman imaging. A modification of this setup by the same group would theoretically allow an acquisition 1000 micrometer sized spots in parallel.[155]

4.4 Line-scan Raman Imaging

One way to increase the acquisition speed of Raman imaging is by acquiring a Raman signal along a line excitation. There are two common ways to generate a line in the sample plane. Today, the most common is by inserting a cylindrical lens into

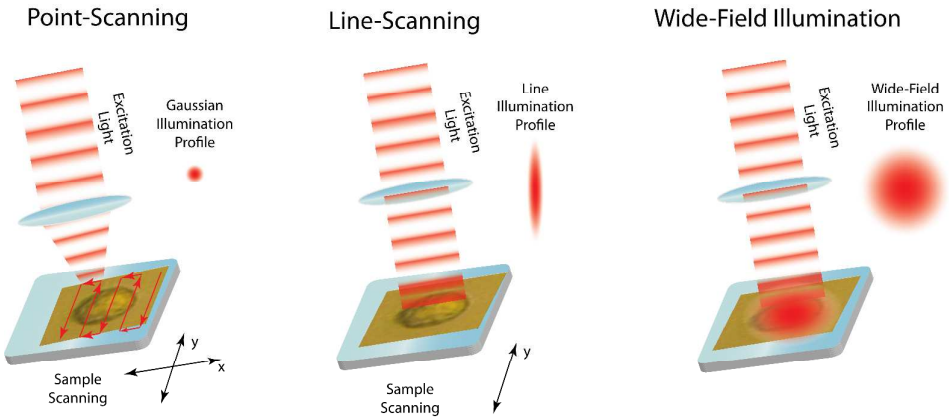

Figure 7: Point-scanning imaging acquisition generates the signal by a Gaussian beam and the sample is raster-scanned in x and y by a motorized translational stage. For line scanning the Gaussian beam is transformed by cylindrical lens and a line profile is imaged into the sample plane. The sample is typically translated in one dimension. In wide-field illumination an expanded Gaussian beam covers a large portion of the sample. A selected Raman band is imaged at once on a CCD detector.

the beam path before the beam enters the objective lens. Due to the cylindrical lens shape a Gaussian beam will be transformed into a line profile, which is subsequently imaged into the focal plane by the objective lens. The Raman signal is generated along every position of the line profile and imaged on the slit of the spectrometer and detected on the CCD camera. Every horizontal pixel line on the detector corresponds to a spatial position in the sample plane. The line size from which the signal is generated is in first approximation only limited by the focal length of the cylindrical lens and the available excitation power to generate a detectable signal. The damage threshold of the sample is also of consideration. The second option to generate a line excitation is by rapidly moving a focal spot using a galvo-mirror along a line. The generated Raman signal is, without passing the galvo-mirror, imaged on the slit of the spectrometer. Because the signal is non-descanned the different position of the spot along the line in the sample plane are imaged to different positions of the CCD detector.

Eysel and Sunder implemented the first line excitation for the investigation of colored solids, in 1980. However, the sample was not mapped, but allowed a sampling of a large portion of the sample at once. *Viers et al.* have also implemented the cylindrical lens approach to generate a line-profile, and used this approach to create hyperspectral maps of micro engineered zirconia.[156] *Ivanda and Furic´* implemented a line-focus approach in a Raman microspectrometer and provided a theoretical description for the line formation.[157] *Drumm and Morris* also used a line excitation scheme to investigate the two-dimensional distribution of polystyrene samples. Most importantly, the researchers introduced principal component analysis as a data analysis tool for hyperspectral data.[158] One of the problems with line-excitation is that the generated line follows a Gaussian profile, resulting in a high intensity in the center of the line and low intensity towards the edges. While it is possible to correct for it by intensity calibration for the uneven illumination profile, it can lead to some problems with the data interpretation. *Christensen and Morris* corrected the uneven illumination by introducing a Powel lens prior the cylindrical lens.[159] A Powel lens creates a top-hat profile of a Gaussian beam, resulting in a quasi-even intensity profile along the line, with a maximum intensity variation of ± 5 %. *De Grauw* suggested that, specifically for biological samples, the implementation of a line scanning based on point scanning can be more advantageous over a line generated by a cylindrical lens.[160] The premier advantage is that the focal spot is diffraction limited, hence providing a better optical resolution, which is crucial for a large variety of biological samples. Bone and polytene chromosome were measured, however, the signal was acquired only along the line, and not in imaging mode.

So far all of the presented realizations of line-scanning Raman microscopes were published before the millennium. In recent years due to advancements in CCD detector technology new line-scanning microscopes were developed with stunning results for single cell imaging. *Hamada* and colleagues developed a line scanning microscope, utilizing a cylindrical lens, and used a laser with a 532 nm excitation wavelength to study single living cells, detecting a signal over a spectral range from 600 cm^{-1} to 3000 cm^{-1}. The researchers were able to perform time-laps images of living cells during cytokinesis. Due to the 532 nm excitation they were able to show the distribution of cytochrome c in single living cells, which corresponds to the distribution of cellular mitochondria.[161] *Oshima et al.* have acquired Raman images of iridocytes in an eye, the spine, and the surrounding muscles of a living medaka fish.[162] This was the first report of spontaneous Raman imaging of a living animal. *Qi and Shih* developed a line-scanning Raman microscope and rapidly imaged bacterial spores and aggregations of microalgae.[163] The researcher also utilized a Powell's lens to overcome the uneven illumination along the line profile. The researchers were able to acquire over 150 hyperspectral images of spores and algae over an area of 80 x 80 µm in one hour. *Schie et al.* have also implemented line-scanning approach and used it to investigate drug-induced changes in living cells.[164]

A very common misperception about line-scanning microscopy is that it increases the acquisition speed when compared to point-scanning microscopy. However, for the same illumination power, and keeping other parameters identical, the integrated Raman signal from a line excitation will be identical to the Raman signal from a point excitation. The speed advantage of the line excitation comes into play when samples with a limited intensity threshold are used. Because, in comparison to point-illumination in line-illumination the intensity is distribute over a much larger area, allowing using higher excitation powers, and hence, reducing the total signal acquisition time.

4.5 Wide-field Imaging

In wide-field imaging, also known as global imaging, the sample is illuminated at once and the Raman signal of a selected band is detected on a 2-D detector. The implemented systems differ primarily in their approach to select the Raman band of interest, which is recorded by the imaging detector. In the simplest approach this is done by narrow-band filter. This, however, is the least flexible approach, because the detection of different vibrational bands requires a manual switching of filters. A further possibility is the selection of vibrational bands using a grating.[165] After the introduction of accusto-optic tunable filter (AOTF) to wide-field Raman imaging by *Treado et al*. this approach for band selection is more frequently used.[166] The first implemented AOTF already provided a wavelength resolution of 2 nm, corresponding to 50 cm^{-1} at an excitation wavelength of 513 nm. Today, AOTFs with much better resolution of < 0.5 nm in the visible range, and 2 nm for the NIR are available. Besides AOTFs liquid-crystal tunable filters (LCTF) have also been implemented to select vibrational bands of interest[167]. *Schluecker et al.* used an AOTF-based wide-field imaging system and compared the performance of point, line, and wide-field imaging modalities, showing that wide-field provides best fidelity images for shorter acquisition times.[168] However, the SNR is better for point and line-scanning Raman

imaging. The switching rate for AOTF are in the low MHz regime, while for the LCTF in the kHz regime, which is more than adequate for imaging of most biological samples. There are a few implementations of wide-field Raman imaging using AOTFs and LCTF for a variety of chemical analysis, such as graphene[169] or explosives[170]. However, this approach has not found broad interest in the biomedical Raman community, yet. Possible reasons could be the high illumination power that is needed, the low damaging threshold, low signal yield from biological samples, and low transmission of tunable filters, in particular for small bandwidths near 5 cm^{-1} for high spectral resolution. The spectral features that are critical for the identification of cells are very minute; hence, spectral undersampling could easily remove important information, making an analysis impossible. Moreover, background contributions are more difficult to correct when only a few spectral data points are available. Another problem with wide-field imaging, which is not related to biological samples, is the resulting uneven illumination of the sample plane, where the signal is highest along the optical axis and decreases significantly of axis.

4.6 Imaging strategies for CRS microscopy

The imaging strategies for coherent Raman methods differ from spontaneous Raman imaging (i) first due to the need of two or more synchronized excitation lasers, (ii) second the coherent and directional emission of the CRS signals, (iii) third by signal magnitude and (iv) by the amount of spectral data points. Therefore, while the faster imaging method of laser scanning is usually employed, in addition to different illumination and detection geometries also several multispectral data acquisition strategies have been developed. In this section we will first summarize the different excitation and detection schemes and discuss their application to biomedical imaging. Afterwards, strategies for sample scanning will be summarized and finally the different approaches for the acquisition of multispectral data are summarized.

4.6.1 CRS Illumination Strategies

Historically, the first CARS microscope as the first implementation of CRS imaging was developed in 1982 by *Duncan et al.* utilizing a Box-CARS illumination configuration depicted in figure 8. CARS is a four-wave mixing (FWM) process, which requires a phase-matching, i.e., momentum conservation, between the four interacting waves. To satisfy this phase-matching condition the Box-CARS geometry is used. This means that the excitation beams, which are used to generate a CARS signal, pass the imaging lens at spatially separated locations and are focused into the sample at an angle to each other. The generated CARS signal exits the sample at a different angle than the excitation light. For image acquisition the laser beam was steered by a pair of galvo-mirrors and focused into the sample plane by a microscope objective achieving a field of view of 200 µm. By underfilling the back aperture of the objective lens the focal spot diameter was 10 µm, hence not diffraction limited. Hence, in the pioneering work the distribution of deuterated water in onion-skin cells was visualized at low spatial resolution.[66] Zumbusch et al. recognized that under a tight-focusing condition, which is achieved through high-NA objective lenses, the phase-matching condition is met.[27] Therefore, the beam propagation can be collinear for illuminating the sample. Mostly, pump and Stokes laser are collinear and co-propagating as depicted in figure 8.

Due to the high NA objective lens the generated wave vector cone contains a large combination of wave vectors that satisfy the phase matching condition in forward direction, while at the same time the short interaction length reduces destructive interference. This is due to the fact, that CARS, RIKE and SRS are non-linear effects. Therefore, the signals are predominantly generated in the focal volume, where the excitation intensities are highest. Thus, to detect CRS signals there is no need for a confocal pinhole, since there are virtually no out-of-focus signals, in contrast to spontaneous Raman. However, the fact, that the signal is mostly generated in forward direction is disadvantageous for imaging thick tissue samples, which is relevant in the context of biomedical applications like intraoperative imaging for surgical guidance. Here, the detection of signal in backward direction needs to be employed, which is called epi-detection. In the following, the different detection schemes of CRS signals will be briefly discussed.

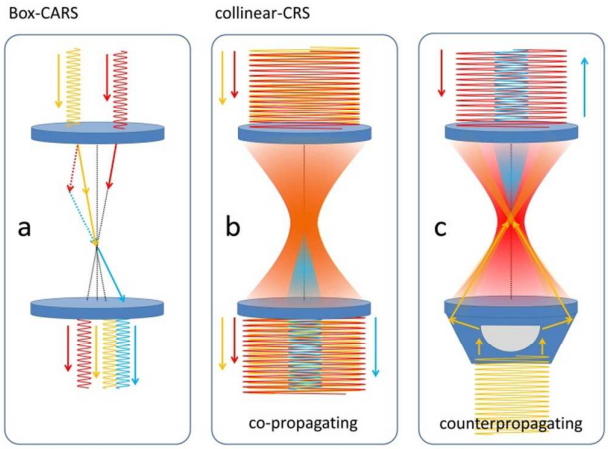

Figure 8: Overview of the different illumination schemes used for CARS and other CRS imaging modalities. The CARS signal is blue, pump laser and Raman loss yellow, Stokes and Raman gain are depicted in red. To satisfy the phase-matching condition for CARS at long interaction lengths and low magnifications, the Box-CARS geometry is used (a). Pump and Stokes-Laser are focused into the sample at an angle to each other for phase matching. Alternatively using high-NA objectives, a collinear illumination scheme is employed (b), since the wave-vector distribution at the focus under the tight focusing condition fulfils the phase-matching condition. Here, pump and Stokes laser are either co-propagating (b), which results in CARS generation in the forward direction, or counter-propagating, generating CARS in the backward direction (c). The counter-propagating illumination scheme is employed in widefield-CARS microscopy.

4.6.2 CRS Detection Strategies

In general, it is possible to detect single band CRS signals in epi-direction using either a non-descanned or a descanned detector or a non-descanned detector in forward direction as depicted in figure 9. Due to the different nature of the signals, the detectors in general but also the optics for epi-detection of CARS and SRS are different. Since the CARS signal is a coherent addition of dipole fields, it is emitted equally strong in forward

and in backward direction for very thin samples. *Volkmer et al.* have shown that while the forward CARS signal increases quadratically with a thicker sample, the epi-generated signal decreases with an increasing sample thickness.[171]

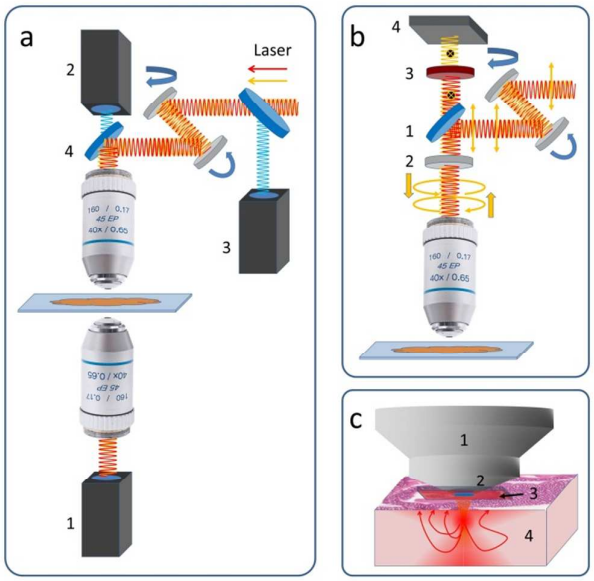

Figure 9: (a) Overview of detection schemes used for single-band CARS and other CRS imaging modalities. Using the common illumination scheme, the CRS signals are predominantly emitted in forward direction and detected by a large area non-descanned detector (1). (a) For CARS imaging of thick tissue samples, epi-detection is employed, using either a non-descanned large area detector (2) or a descanned detector (3) and appropriate filters (4). (b) Epi-SRS requires a polarizing beam splitter (1) and a quarter wave plate (2) changing the polarization of incoming and backscattered lasers by 90°, such that the Raman loss signal is passing the filter (3) and detected on a large photodiode (4). (c) Alternatively, a large area diode detector (2) is covered by a filter (3) and directly attached to the objective (1) for the detection of scattered laser photons.

This is primarily due to the increasing phase mismatch in the backward direction of signal generation and the resulting destructive interference, when utilizing the most common collinear illumination with co-propagating pump and Stokes lasers as depicted in figure 8. Since the epi-signal is typically generated from small structures or interfaces but not from the bulk medium which generates a strong non-resonant background in forward-direction, the epi-signal allows for high-contrast imaging of small structures depicted in figure 10. Forward and epi-CARS images of lipid droplet accumulations in adipocytes differ. Epi-CARS highlights small lipid droplets. However, when imaging ~100 µm thick samples, the major contribution to the epi-signal are back-scattered and back reflected photons, which were initially generated in forward direction.[25] In order to realize epi-SRS detection, two approaches have been realized.[26, 121] First, the backscattered laser can be separated by polarization using a quarter wave plate and a polarizing beam splitter to change the polarization of excitation and back-reflected laser light by 90°. The polarizing beam splitter directs the backscattered light onto the detector (figure 9 b).[121] Alternatively, the Raman-Loss signal is detected using scattered photons only. Here, a large area photodiode covered with a filter to reflect the Stokes laser is directly attached to the objective lens. A hole in the center of the diode allows the excitation light to pass (figure 9 c).[26] This design enables video-rate SRS imaging in epi-direction, but requires custom designed coated diode-detectors.

Schie et al. implemented an approach to detect both forward and epi- generated CARS signal on the same detector.[172] The forward generated signal was collected by a condenser lens, temporally delayed, and reflected back into the objective lens. The epi-generated signal was collected by the same objective lens. Both signals were detected on the same avalanche photo diode, and sampled by a time-correlated single photon counting (TCSPC) board. Due to the temporal separation of the arrival time, it was possible to separate the signals though time gating, figure 10.

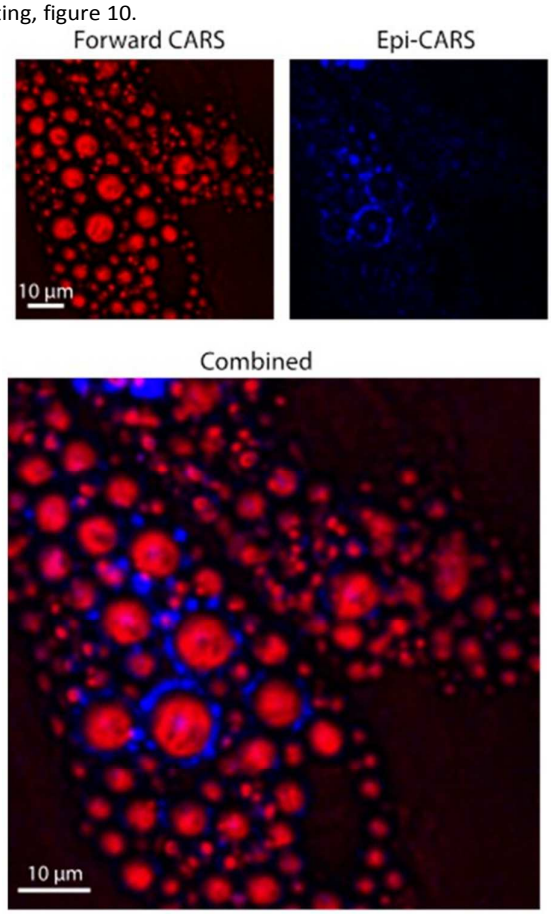

Figure 10: Forward and epi-CARS images of lipid droplet accumulations in adipocytes. Both signals were detected simultaneously on the same detector. Due to the temporal separation between the two signals in this specific arrangement, the signals were detected by an avalanche photo diode and separated based on their arrival time using time-correlated single photon counting (TCSPC).[172] (Reprinted with permission from I. W. Schie, T. Weeks, G. P. McNerney, S. Fore, J. K. Sampson, S. Wachsmann-Hogiu, J. C. Rutledge and T. Huser, Optics express, 2008, 16, 2168-2175. Copyright 2008 Optical Society of America.)

For biomedical imaging applications, epi-detection is by far the preferred detection scheme. In addition, high-speed image acquisition is crucial in order to follow fast processes in living organisms in real time, e.g., trafficking of lipid droplets.[110] Therefore the next paragraph will focus on imaging strategies.

4.6.3 Sample scanning strategies for CRS imaging

While *Duncan at al.* already used fast laser scanning in 1982,[66] *Zumbusch et al.* and *Hashimoto et al.* used a piezo-activated translational stage to scan the sample over the excitation beam with a pixel dwell time of 10 ms for implementing CARS microscopy in the collinear beam geometry.[27, 173]. While sample scanning by piezo-activated translational stages has the advantage to operate the objective lens on the optical axis for best optical performance, this scanning method is slow and unsuitable for living biological samples. The imaging speed can be significantly improved through laser-scanning microscopy (LSM), using a pair of fast-scanning mirrors.

In LSM a pair of scanning mirrors steers the excitation beams by changing the deflection angle. Scan and tube lens subsequently image the beams on the back aperture of the objective lens. While the beam remains stationary on the back aperture of the objective lens, it changes the entrance angle. This change in angle on the objective back aperture results in a change of the focal position in the focal plane (figure 11). An excellent overview on constructing a steerable beam can be found by *Fällman and Axner*.[174] *Cheng et al.* implemented a LSM for CARS microscopy of biological samples.[175] Using this approach, the acquisition times for eukaryotic cell could be reduced to ~ 10 s which was a significant improvement in comparison to piezo-stage scanning. Today LSM is the most common implementation for CARS microscopy. There are two implementations of galvo scanners, which differ in the scanner of the fast axis. Nonresonant laser scanners routinely used in LSMs provide scanning speeds of up to 1200 lines per second, but the angular deflection is linear in time and the line scan speed can be changed. Resonant scanners on the contrary are much faster, e.g., 8-12 kHz, enabling video rate image acquisition.[26] However, the scanner can only operate at a fixed line frequency and the scanner motion is sinusoidal. Therefore, the scanner is used in the central angle range, where the motion is nearly linear. An alternative fast scanning option has been implemented by *Evans et al. In-vivo* video-rate CARS microscopy in epi-direction has been realized using a polygon-scanning mirror[22]. In polygon mirror scanning the fast axis is sampled by polygon mirror allowing a very rapid scanning along on dimension, while a galvo-scanning mirror translates the beams of the slow axis. The deflected beam is imaged by scan and tube lenses onto the back aperture of the objective lens. Each deflection angle corresponds to a spot position in the sample plane (figure 11). *Evans* used this approach for *in-vivo* imaging of lipid rich structures such as sebaceous glands, adipose tissue, and corneocytes in the ear-skin of a living mouse at a pixel dwell time of 160 ns. The same scanning method is also used by other groups for fast imaging.[38]

A different approach to increase the imaging acquisition speed was proposed by *Minamikawa et al.*[176] using a multi-focus illumination. The researchers created multiple foci using a micro-lens array. By spinning the micro-lens array and imaging seven beamlets into the focal volume the researchers achieved an acquisition speed of 30 fps for polystyrene beads and 10 fps for HeLa cells. An increased number of beamlets is expected to further increase the multiplex effect and faster acquisition rates.

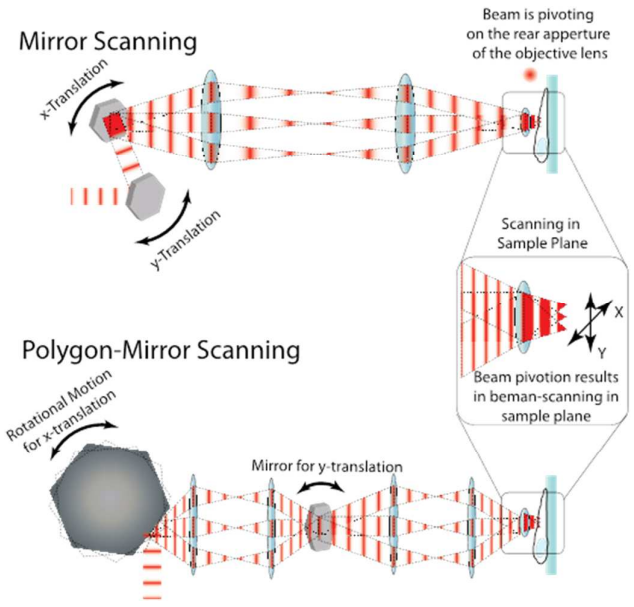

Figure 11: Laser-scanning microscopy as the most common implementation of CARS imaging. A pair of galvo-mirrors is used to steer the excitation beam. Two relay-lenses image the scanning entrance aperture on to the back aperture of the objective lens. Because the beam is at rest in the entrance aperture, in the conjugated plane the beam is pivoted on the entrance aperture of the objective lens resulting in beam scanning in the object plane. In scanning with a polygon mirror the fast axis is replaced by a rapidly rotating polygon mirror allowing faster acquisition speeds as with galvo-scanning mirrors.

Heinrich et al. presented the first implementation of a wide-field CARS geometry for CARS imaging acquisition.[177] To satisfy the phase-matching condition the approach uses counter-beam propagation of the pump beam and the Stokes beam depicted in figure 8. The Stokes beam is coupled through a conventional objective lens, whereas the pump beam is imaged into the sample plane through a dark-field condenser lens. With this configuration an effective area of 60 μm^2 could readily be imaged with an exposure time of 60 s using a high power ns-pulse excitation laser source delivering 0.5 mJ of energy in the sample plane. In a follow-up publication the researchers acquired readily fair-quality CARS images of lipid vesicles from a single shot corresponding to an exposure time of 3 ns[178] and from cellular lipid droplet accumulations.[179] *Toytman et al.* implemented a similar wide-field approach and were able to acquire images of polystyrene beads with an acquisition time of 1 ps, and lipid-rich myelin sheaths.[180] Despite the rapid imaging advantage the utilized power in the sample plane are still of concern for living biological samples. In the same publication *Toytman* compared the total fluence for their wide field approach on myelin sheaths, which was 10

Jcm^{-2}, to the fluence for a LSM-CARS acquisition, which is around 0.3 Jcm^{-2}. Furthermore, so far epi-detection is not yet possible with wide-field CARS, but required for imaging thick samples.

Heuke and coworkers developed a theoretical and experimental implementation for Bessel-beam CARS illumination for an axial profiling of multi-layer structures.[181] Using numerical data they were able to show that it is possible to reconstruct a depth profile of a structured sample using the Bessel-beam by solving the inverse scattering problem. This work could lead to rapid 3-D profiling of the sample without the need for focal changes.

Fast imaging of biological samples acquiring 30 frames per second has been realized using intense C-H or O-H stretching vibrations,[25, 26, 121] however, the chemical contrast is limited, when only single Raman resonances are used. For a chemical characterization of complex biological samples and the identification of several marker molecules, either several selected[26] resonances or a spectral region need to be used.[121] In the following section different strategies for the acquisition of multi-spectral data will be summarized.

4.6.4 Multispectral imaging strategies

In order to acquire spectral data using CRS, there are two strategies: hyperspectral and multiplex imaging depicted in figure 12 (see also section 3.2). Hyperspectral imaging is based on single band CRS. The sample is illuminated with two synchronized lasers generating CARS, Raman gain and Raman loss, when the difference frequency of both lasers matches a Raman-active vibrational frequency of molecules present in the laser focus (figure 12 a). By subsequent image acquisition at different Raman resonances, which is realized by tuning the frequency difference between pump and Stokes-laser, hyperspectral imaging is realized (figure 12 b). Here, images at different Raman resonances are acquired. The advantage of hyperspectral imaging relies on its experimental simplicity, since no spectrometer is needed. Furthermore, the signals can be collected in epi-direction, which is important for *in vivo* imaging.

However, scanning the laser wavelength is restricting the imaging speed, since OPO-systems require several seconds for wavelength changes, thus several minutes for a hyperspectral image stacks.[37, 73, 182, 183] Therefore, fast implementations of hyperspectral Raman imaging depend on fast wavelength scanning laser sources. Using a fast wavelength-swept fiber laser, CARS spectra covering 150 cm^{-1} can be acquired within 1.2 ms.[93] Novel laser concepts (see also section 3.1) will significantly increase the speed of wavelength sweeps. Using the tuning range of an Yb-laser, *Ozeki et al.* realized 2800-3100 cm^{-1} hyperspectral imaging of tissue acquiring 91 images within 30 seconds using a custom build wavelength scanner consisting of a grating for dispersing the laser beam and a galvoscanner.[121] By applying the method of spectral focusing introduced by *Hellerer et al.*[97] *Fu et al.* acquired 60 frames from 2810 and 3088 cm^{-1} at 1.12 s/frame acquisition speed[34, 184]. Recently, using a special laser for time encoded Raman SRS spectra covering 100 cm^{-1} where acquired within 157 µs only.[109]

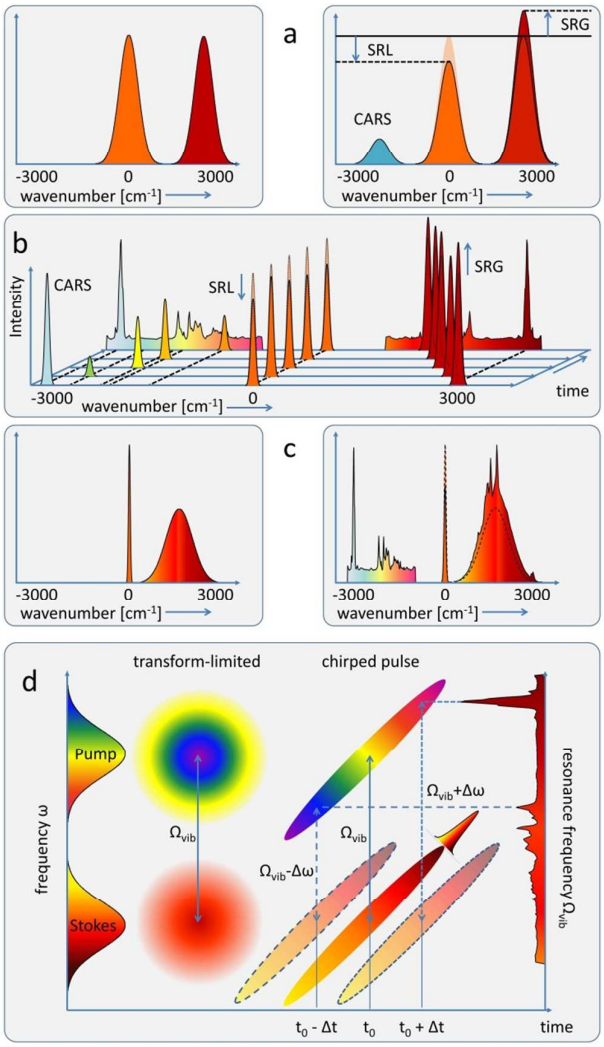

Figure 12: Overview of methods for the acquisition of spectral data. (a) single band CRS, left illumination, right detection. (b) Hyperspectral Raman imaging is sequential scanning of several Raman resonances, (c) while the simultaneous acquisition of CRS spectra in every pixel is called multiplex CRS. (d) Spectral focusing enables high spectral resolution imaging and fast spectral tuning by changing the pulse delay utilizing broad band pulses which are equally chirped.

In contrast, multiplex CRS imaging relies on the acquisition of CRS spectra at each pixel as introduced in 2002.[185] Except for one approach using tuned amplifiers for multiplex SRS[39] and multiplex RIKE,[30] multiplex CARS is predominantly used and manifold biomedical applications have been reported.[186-194] Here, the sample is illuminated with broadband lasers in order to acquire a significant part of the Raman spectrum. With this method, CARS spectra of biological samples have been acquired within 3.5 ms covering 600-3400 cm^{-1}.[40] While multiplex CARS provides broad spectral coverage, forward detection is not possible in thick tissue specimen, while using a spectrograph prohibits the detection of non-ballistic scattered signal photons. Furthermore, the spectral line shapes are

distorted due to interference effects, such that phase retrieval methods are needed in order to extract the Raman spectrum. Here, two approaches based on the maximum entropy method and the Kramers-Kronig relations have been reported.[195, 196] Since an in-depth description of broadband CARS microscopy approaches is beyond the scope of this review, further details on multiplex-CARS imaging can be found in recent reviews.[194, 197] Further implementations of broadband coherent Raman imaging include broadband single pulse CARS in combination with pulse shaping techniques, which are currently experimentally too complex for biomedical applications.[41-46, 198]

Another technique using broad band laser pulses is called spectral focusing depicted in figure 12d. This method combines the advantages of hyperspectral and multiplex CRS imaging enabling fast spectral scanning and high spectral resolution imaging by using broad band lasers and a point detector, hence circumventing the need for a spectrograph. In order to increase the spectral resolution the broadband laser pulses are equally chirped, such that the spectrograms of both pulses are parallel, which can be achieved either by using a pulse stretcher[97, 98] or by passing both pulses through a thick piece of glass.[96, 199-201] Hence, when both stretched pulses overlap in time, the high frequency components of the Pump pulse overlap with the high frequency components of the Stokes pulse only, such that the actual spectral resolution is improved to that of a transform limited pulse of the pulse duration of the chirped pulse.[201] Spectral tuning covering the spectral width of the pulses is simply achieved by changing the pulse delay. Hence, this concept allows adjusting the spectral resolution from 5 to 400 cm^{-1}, when combining a 60 fs Ti:Sa pump with a SC from a PCF. A tuning range from 2500 – 4100 cm^{-1} has been realized.[200] However, when the spectral resolution is increased, the peak intensity is reduced by the same factor. This approach provides a simple method to adapt the spectral resolution and peak power to the specific needs of the imaging experiment.

5. Biomedical applications

5.1 Cell studies

Before Raman imaging studies of single cells are presented, a typical Raman image of fibroblast cells is presented in figure 13. The data were taken from a paper about the detection of stress induced changes at the subcellular level by Raman microscopy[202]. The data set was collected with a step size of 1 µm. The Raman spectral contributions of aqueous buffer were removed by subtracting an average spectrum of the surrounding medium. The cell spectra were segmented by k-means cluster analysis into groups according to their similarity. The plot of the cluster membership function indicates the cell nuclei (red) of two adjacent cells, the cytoplasm (blue) and lipids droplets (green) that are not fully resolved at this resolution. More than 40 bands are labelled in the mean cluster spectra. Spectral contributions are assigned to proteins, lipids and nucleic acids as summarized in table 1.

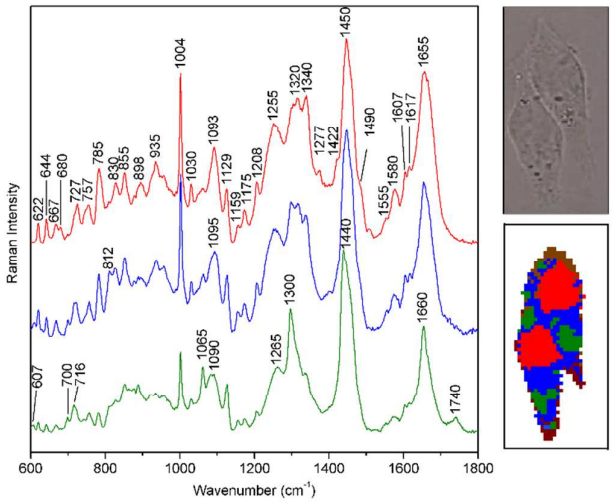

Figure 13: Raman image of single fibroblast cells: K-means cluster analysis segments the data set into cell nuclei (red), cytoplasm (blue) and lipid droplets (green). Bands are labelled in mean cluster spectra (shifted to avoid overlap).

Some bands overlap and can be assigned to more than one component. Because peptide groups and aliphatic groups in amino acids are abundant in proteins, these bands dominate. Bands of aromatic amino acids are well resolved due to the small bandwidth. Most intense lipids bands are due to fatty acids chains, in particular between 1000 and 1700 cm^{-1}. Prominent nucleic acid bands are assigned to the phosphate backbone and nucleobases. They are usually less intense than protein and lipid bands in cells and tissues (see 5.3). Usually, the cell number of Raman imaging cell studies are low because data acquisition by spontaneous Raman scattering is relatively slow. Using state-of-the-art instrumentation acquiring 1000 spectra per image at a step size of 0.5 µm and with 0.5 s exposure time gives typical total exposure times of more than 10 min (500 s plus additional time for moving the sample or scan the laser and saving the spectrum). The cell number ranged from six to study changes in stressed cells in 2006 as shown in figure 13[202], 48 to classify tumor cells in 2010[203] and 70 to monitor the lipid uptake in macrophages in 2012.[204]

An interesting feature in the paper about identification and differentiation of single cells by Raman imaging[203] was the classification of four cell types: leukocytes from peripheral blood, leukemia cells OCI-AML3, and breast cancer cells MCF7 and BT-20. Many papers just reported the distinction of two cell types which does not exploit the full potential of the Raman fingerprint property. The advantage to collect Raman images instead of single spectra per cell (as presented in 5.2) is that the data encompass intra-cell variations as presented in figure 13. If only one spectrum per cell is collected, intra-cell variations that occur for different positions within the cells might overlay with inter-cell variations that are specific for each class.

Table 1: Assignment of typical Raman bands from cells and tissues. Abbreviations: lipid (L), phospholipid (LP), protein (P), nucleic acid (N), backbone (bk), deformation (def), phenylalanine (Phe), tyrosine (Tyr), tryptophan (Trp).

	Assignment	Bands (cm^{-1})
L	Cholesterol	607, 700, 1440, 1674
P	Phe	622, 1004, 1030, 1159, 1208, 1607
P	Tyr	644, 830, 855, 1175, 1617
N	Thymine	667, 757, 780, 1277
N	Guanine	680, 1490, 1580
L	$N(CH_3)_3$	716, 875
N	Adenine	727, 1490, 1580
P	Trp	757, 1159, 1340, 1555, 1617
N	Cytosine, bk	785
N	Bk (RNA)	812
P	Peptide C-C_α	898, 935
L	C-C chain	1065, 1129
PL	PO_4^{2-}	1090
N	Bk (PO_4^{2-})	1093-1100
P	Amide III	1255
L	C=CH	1265
L	CH_2 def.	1300, 1440
P	CH_3 def.	1320, 1450
N	CH_2	1422
P	Amide I	1655
L	C=C	1660
L	C=O	1740

Raman spectra of lipids share many similarities, in particular, if they differ by just few alkene groups (CH_2) in fatty acid moieties. A strategy to monitor the uptake of a defined lipid class is to introduce deuterium labels. The higher mass of deuterium compared to hydrogen shifts the positions of hydrocarbon vibration to lower wavenumbers. This strategy was employed to monitor the time-resolved uptake of serum-albumin complexed palmitic acid, oleic acid, cholesterol[204] and arachidonic acid[205] in macrophages.

A versatile and powerful approach in single cell studies is the combination of fast CRS imaging with chemically highly selective Raman spectroscopy, which ideally complement each other.[206] The combination of SRS with spontaneous Raman spectroscopy enabled the identification of cholesterol ester as a marker for aggressive prostate cancer.[207] This finding was not possible with single color CARS or SRS imaging, nor with Raman spectroscopy alone. Similarly, the combination of CARS microscopy and Raman spectroscopy has been applied to study lipid droplets in individual cells.[208, 209] First, CARS imaging was used to resolve individual lipid droplets in single cells at high speed. Then, Raman spectra of these droplets were collected in order to determine the lipid composition. The fatty acids palmitic acid and oleic acid were distinguished by characteristic Raman bands of carbon double bonds and the lipid composition was determined by asymmetric least squares fitting of pure fatty acid spectra. These studies clearly demonstrate the benefit of combining Raman spectroscopy with CRS imaging to address important biomedical problems.

5.2 Laser tweezers Raman studies

The application of laser-tweezers offers a large number of advantages in Raman microspectroscopy (see also section 4.2). Besides allowing micromanipulation of single cells and measurements of mechanical properties accompanied by chemical information in single cells, optical tweezers also allow a rapid cell sorting after a spectroscopic identification. Moreover, because the position of the trap can be moved along the z-axis, a further reduction of background contributions from substrates can be achieved. The group around Y. Q. Li implemented the first laser-tweezers Raman spectroscope to differentiate between red blood cells (RBCs) and yeast cells, [210] and was instrumental in establishing LTRS as an valuable tool in the Raman field. In a follow-up publication by the same researchers LTRS was combined with shifted-excitation differences to reduce glass background contributions.[211] The system was used to study heat-induced protein degradation in trapped *E. coli* cell and the improvement of background correction through shifted excitation was shown on RBCs and on yeast cells. The characterization of *E. coli* cells and bacterial spores with LTRS has also been done by others, showing superb differentiation between different strains.[212, 213] *Chan et al.* have shown excellent separation of individually trapped leukemia T and B cells of healthy patients and leukemia patients, resulting in average cell classification accuracies of 90 % and 95 % for healthy and leukemia patents, respectively.[214] LTRS has also been used to investigate the effects of cell fixative on the molecular information of single cells;[215] the effects of chemotherapeutic induced effects in cells [216]; and monitoring of apoptotic and necrotic stages in cell [217]. Besides singe cells, *Tang et al.* also investigated swelling properties of viable mitochondria. [218] *Fore et al.* have shown that leukocytes are commonly trapped by their nuclei,[219] which could potentially result in a bias when using cells that have smaller nuclei or presence of other dense cellular compartments, such as intracellular lipid droplets.

While multiplexing the number of traps that can capture cells in parallel can help for stationary located cells in a sample dish, the sorting of a large number of cells remains non-trivial with this approach. A viable option to improve sorting of cells is to use microfluidic devices. Microfluidic chips have been used for cell trapping experiments early on in LTRS. *Ramser* and co-workers used LTRS in a microfluidic device to investigate oxygenation properties of trapped red blood cells that were exposed to different chemical environments delivered through the microfluidic channel.[220] The first true Raman activated cell sorting (RACS) was implemented by *Lau et al.*, showing with a proof-of-principle experiment that cells, B cell lymphoma and T cell lymphoblast, can be identified in an microfluidic environment, and sorted into different chambers.[221] The researcher used a trap-and-release approach and determined the relation of trapping power to flow velocity for beads and leukemia cells. With a trapping power of up to 25 mW @ 785 nm, cells could be trapped at fluidic velocities of ~ 400 µm/s. The flow inside the chip, however, was not easily controllable

due to the use of a gravity injection system. *Dochow* and colleagues developed an advanced microfluidic chip, where a microfluidic pump controls the flows inside the chip. Cells were trapped by a laser with 1070 nm excitation, the Raman signal, however, was probed by a 785 nm laser.[222] In contrary to a conventional implementation LTRS the optical trap was built in a counter propagating geometry. The trapping geometry was tested in a square quartz capillary on three different cell-types, with an overall cell identification accuracy of ~ 92 %. In the microfluidic chip the overall cell identification accuracy was ~ 95 %. In a follow-up publication *Dochow et al.* have improved on the design, by implementing a quartz window on the microfluidic chip, trapping individual cells manually with the 1070 nm laser, and acquiring Raman spectra of trapped cells with the 785 nm laser.[223]

5.3 Tissue and biopsy studies

Before examples of Raman imaging studies of tissue sections are presented, a typical Raman image of brain tissue is shown in figure 14. The data were taken from a paper about high resolution Raman microspectroscopic imaging of brain tumors[224]. The small step size of 2 µm in combination with bilinear decomposition of the data matrix by vertex component analysis enabled to distinguish cell nuclei, brain tissue and microcrystals that were formed by oversaturating conditions during the drying process.

VCA identifies the most dissimilar spectral components and uses them for reconstruction of the data sets with non-negativity constraints, that means both the components and the abundances are positive. Among the advantages of the described VCA implementation are that no preprocessing was required (such as baseline correction, normalization or smoothing) and results are chemically significant. Comparison of the microcrystal component with a reference spectrum reveals that the microcrystals are composed of cholesterol.

The tissue component contains spectral contributions of lipids and proteins. The cell nuclei component contains spectral contributions of proteins and nucleic acids similar as for nuclei in single cells shown in figure 13. The absence of the band near 680 cm^{-1} and the shift of the phosphate backbone band to 1098 cm^{-1} are consistent with structural distortions of B-DNA due to drying. The cell nuclei abundance plot coincides very well with the H&E staining of the tissue section after the Raman data acquisition. In follow-up studies, non-dried brain tissue sections were immersed in aqueous buffer during Raman imaging. This prevents drying induced artefacts such as crystallization and denaturation of biomolecules. Eight Raman images from five specimens were combined and analyzed by VCA and the related algorithm N-FINDR. Beside proteins, lipids, nucleic acids and buffer, cholesterol ester and carotene were identified[224]. 39 Raman images were collected from six glioma brain tumor specimens with tumor grade ranging from WHO II to WHO IV[225]. The abundance plots of the cell nuclei were processed by an image segmentation procedure to determine the average nuclei size, the number of nuclei and the fraction of nuclei area. The latter two morphological parameters correlated with the malignancy. A combination of bilinear decomposition and non-negativity constrained linear least squares fitting was introduced to assess chemical parameters. Whereas the protein content was almost unchanged, nucleic acid content, lipid content and lipid to protein ratios correlated with the malignancy.

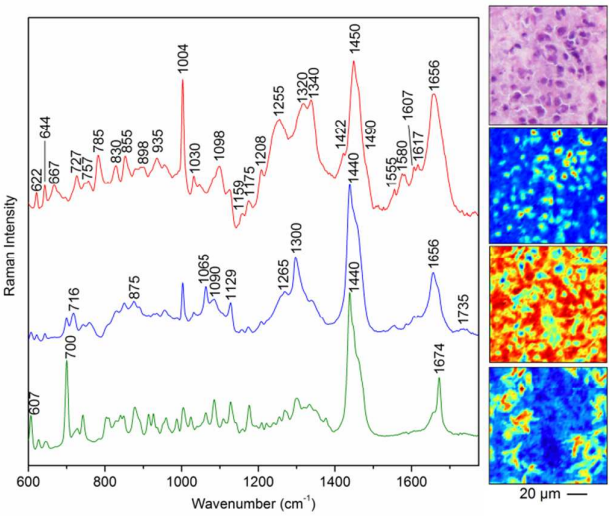

Figure 14: Raman image of brain tissue section: vertex component analysis decomposes the data set into cell nuclei (red trace), tissue (blue) and microcrystal (green). Bands are labelled in component spectra (shifted to avoid overlap). Images display the abundance of each component (from bottom to top): microcrystal, tissue and cell nuclei that correlate well with tissue section after H&E staining.

Diagnostic prospects of Raman imaging were demonstrated for the determination of the primary tumor of brain metastases[224]. In a considerable number of cases, brain metastases cause clinical symptoms before the primary tumor, and screening by imaging modalities, histopathology and immunohistochemistry fails to give accurate findings. Because Raman spectra provide molecular fingerprints of tissues, this approach provides complementary information. First, cluster membership maps of Raman images were correlated with consecutive H&E stained tissue sections to annotate the clusters. Second, the confirmed cluster assignments trained a support vector machine (SVM) to distinguish normal brain, necrosis, carcinoma and other tissues in Raman images of 22 specimens. Then, a second level SVM discriminated brain metastases of bladder carcinoma, lung carcinoma, mamma carcinoma, colon carcinoma, prostate carcinoma and renal cell carcinoma.

Long exposure times are also limiting factors in Raman imaging of tissues. To overcome this problem, autofluorescence was suggested as a sensitive but low specific technique for prescreening and selecting regions of interest for subsequent Raman spectroscopic assessment[226]. This combination has been demonstrated for basal cell carcinoma in skin tissue sections and enabled accurate detection of tumor margins.

In principle, CRS is another candidate to speed up data acquisition in tissue studies.

5.4 Whole organ and animal studies

Raman systems coupled to fiber probes usually collect a single spectrum per exposure, even if multiple fiber cores are used. For fiber optic Raman imaging (i) anaesthetized small animals are moved by a x-y stage [227], (ii) the probe is moved over a region of interest[228], (iii) a fiber array is coupled to a multi-channel Raman spectrograph[229] or (iv) individual fibers in an imaging bundle are subsequently addressed by a scanning device [230]. Approach (i) was experimentally realized by a lensed fiber probe that focused the 785 nm laser excitation onto a spot of 120 µm. Images were sequentially collected in a raster scan mode with 100 µm step size and 4 second exposure time per spectrum. Brain tumors and tumor margins were detected under a cranial window in an *in vivo* murine model by Raman imaging. A bi-modal probe was introduced in approach (ii) for simultaneous fluorescence lifetime and Raman imaging. The probe was also tested on mouse brain. Both modalities showed contrast for bone, brain tissue and blood vessels. The FLIM setup operated at an acquisition rate of 10 kHz. As Raman imaging with short exposure time of 20 ms gave poor quality spectra, integration time was increased to 1 s for additional spectra at selected points. The array in approach (iii) encompassed 20x20 fibers which enable simultaneous acquisition of 400 individual Raman spectra with exposure times down to 1 second. A key element was a multichannel spectrograph with a large array CCD detector that was developed for astronomical applications. Approach (iv) designed CARS imaging fiber probe consisting of 10000 coherent light guiding elements preserving the spatial relationship between the entrance and the output of the fiber. The scanning procedure can be shifted from the distal to the proximal end of the fiber probe. This offers a convenient solution towards CARS and other multiphoton endoscopy.

Strategies were described for small animal optical imaging based on Raman spectroscopy and Raman-active nanoparticles[231, 232]. Because spontaneous Raman scattering is a weak process, surface enhanced Raman scattering (SERS) nanoparticles (NPs) and single-wall carbon nanotubes (SWNT) were used to demonstrate deep tissue, whole body Raman imaging, NP pharmacokinetics, multiplexing, and in vivo tumor targeting using a system adapted for small animal Raman imaging. SWNTs show intense resonance enhanced Raman signal. Tumor targeting was reported for tripeptide RGD functionalized SWNTs[231]. After intravenous injection, Raman imaging commenced over the next 172 hours and revealed increased accumulations of RGD-SWNTs in tumor as opposed to plain-SWNTs. If reporter molecules are bound to gold of silver NPs, the Raman signals of the reporter molecules can be sensitively detected. Different reporter molecules give fingerprint-like SERS spectra which offer extremely high multiplex capability using a single wavelength of excitation. Such NPs were applied to a Raman-based strategy for multiplexed molecular imaging[232]. 326 fM concentration of SERS-nanoparticles were detected and ten variations of co-localized SERS nanoparticles could be unmixed. Another feature of the presented noncontact Raman endoscope was that it has been designed for efficient use over a wide range of working distances from 1 to 10 mm.

The group of Gellermann et al. published a series of papers about Raman imaging detection of the macular carotenoid pigment that is present at high concentration in the retina of human eyes[233]. Instead of NPs or SWNTs, carotenoids can be sensitively detected by Raman spectroscopy under resonant excitation that means near electronic excitation at blue wavelengths. The experimental Raman imaging setup routed light from a mercury arc lamp via a fiber bundle into a light delivery and collection module. The light is spectrally filtered at 488 nm with a 1 nm bandpass filter and imaged onto a 4 mm diameter spot centered on the fovea of an excised eyecup. The light scattered back from the retina is filtered at the C=C stretch band near 1524 cm^{-1} (527 nm in the case of 488 nm excitation) and imaged onto the 375x241 pixel array of a CCD camera. This setup without a laser for excitation and spectrograph for dispersion is quite unusual for Raman imaging.

Ji et al. previously demonstrated that in vivo SRS imaging in reflection mode with solid state lasers and free-space optics is feasible in simulated surgical conditions in mice bearing human gliomas where blood, dissected and/or coagulated tissue and movement associated with respiratory and cardiac cycles are present [234] SRS microscopy differentiated healthy brain tissue from tumor-infiltrated brain based on histoarchitectural and biochemical differences. Differentiation was achieved by different lipid to protein content that were assessed by SRS signals at 2930 and 2845 cm^{-1}. A linear combination method extracted the lipid and protein distributions from two-channel SRS images and displayed them as color-coded images that visualized cell bodies as well as extracellular structures.

5.5 Vibrational labelling techniques for biomedical applications

While label-free tissue analysis is the key strength of Raman based imaging techniques, the specificity for differentiating biomarkers, which share many structural elements, e.g., lipids and proteins, is limited. In order to trace a specific molecule, labelling is required. While the key technique for labelling is fluorescence, small molecules like water cannot be labelled efficiently, since the fluorescent tag increases the molecular size and weight, hence its diffusion properties, but also other properties like acidity and reactivity. Here vibrational labelling is advantageous, since common labels like alkyne and deuterium are very small and hence preserve the molecules' properties. Hence, studies of cellular hydrodynamics rely on monitoring the uptake and release of heavy water.[58-60]

In order to maximize the contrast, the marker band resides in the vibrationally silent region of the Raman spectrum around 2200 cm^{-1}. This approach enables the background free detection of the molecular marker in low concentrations. Alkyne tagging has been employed to study the distribution and synthesis of DNA, RNA, proteins, phospholipids and triglycerides.[56, 62, 63] Multiplexing can be realized by using isotope labelling of the alkyne tag, such that three different tags can be detected in the range from 2048 to 2125 cm^{-1}.[63] Alternatively, substituting hydrogen by deuterium shifts the

strong CH-stretching vibration to 2100 cm-1, while the chemical behaviour is almost not affected. [61, 62, 64, 184, 204, 235] In figure 15 the uptake of CD-labelled lipids by macrophages is monitored over time to study the intracellular lipid metabolism in macrophages.

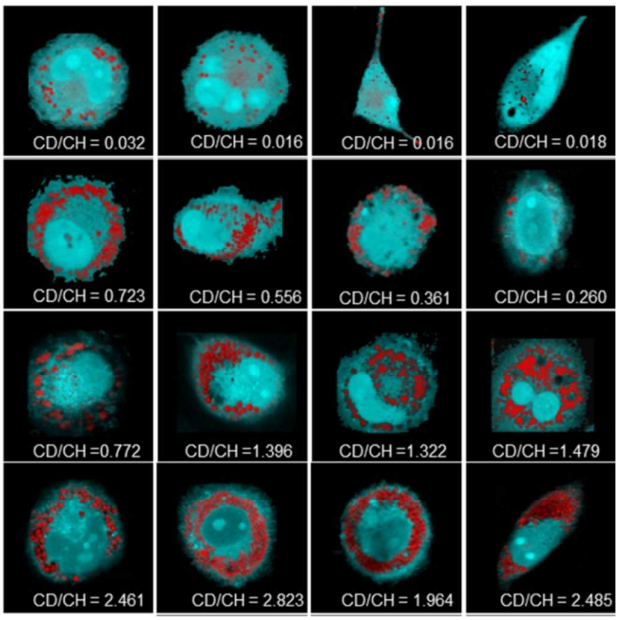

Figure 15: Raman images to study the intracellular lipid metabolism in macrophages. The uptake of deuterium labelled lipids is monitored over time by Raman imaging (red). Upper row 30min, second row 6 h, third row 24 h, fourth row 30 h.[204] (Reprinted with permission from C. Matthäus, C. Krafft, B. Dietzek, B. R. Brehm, S. Lorkowski and J. Popp, Anal. Chem., 2012, 84, 8549-8556. Copyright 2012 American Chemical Society.)

5.6. CRS imaging of drug delivery systems

Another important biomedical application requiring fast label-free imaging is studying the uptake and distribution of drugs, since the efficacy of a medical treatment highly depends on the delivery of the drug to the target structure. Since many drugs are small, label-free or labelling with small tags is required, in order to preserve the transport properties of the drug.[184, 235-242] The so far reported manifold applications include drug delivery to the skin,[240, 243] monitoring changes upon dissolution and the impact of the composition on the drug release [237-239]. The complex of Raman imaging of drug delivery systems has been reviewed recently.[241]

5.7 CRS imaging for label-free histopathology

Another important application of CRS is the label-free visualization of tissue pathologies.[193, 244, 245] CRS enables to visualize the morphology and the chemical composition of tissue, either using CRS alone or in combination with other nonlinear imaging modalities like second harmonic generation (SHG) and two photon excited fluorescence (TPEF) as shown in figure 16. Here, hematoxylin and eosin stained tissue sections are compared to label-free multimodal CARS-SHG-TPEF imaging of the identical section displaying the colon of a mouse. CARS has been performed at 2850 cm^{-1} to visualize the lipid distribution (red channel). Areas as large as 1 cm^2 can be analyzed within minutes. The capability to investigate native tissue is promising for intraoperative imaging in the future.

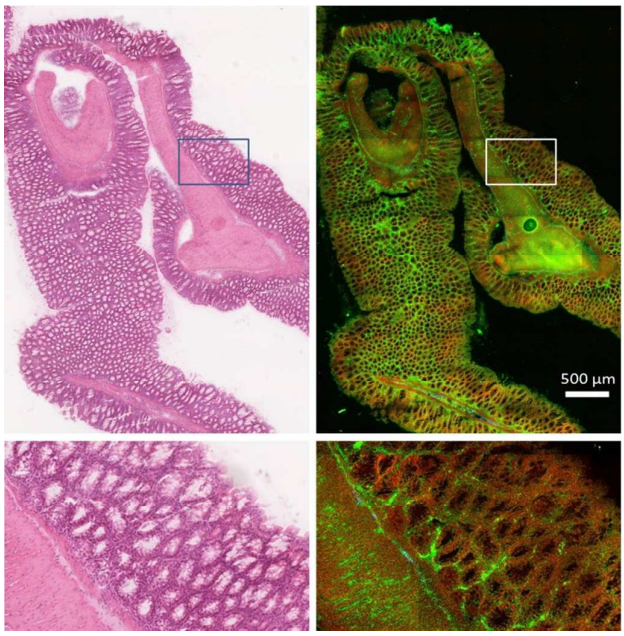

Figure 16: Comparison of an H&E stained image (left) with a multimodal nonlinear image (right) combining CARS at 2850 cm^{-1} (red), SHG (blue) and TPEF (green) of the colon of a mouse. The label-free multimodal image reproduces the tissue morphology similarly accurate as compared to the H&E stained image.

6. Conclusions

The field of spontaneous and coherent Raman scattering microscopy extensively expanded within the last twenty years. The current contribution focused on developments in instrumentation and methodologies that are prerequisites for new applications. As the number of papers is already too large for a comprehensive summary – even if limited to imaging for biomedical applications – the reader is referred to recent reviews that summarized other reviews and relevant papers. Unmet needs exist in particular in biomedicine, clinical diagnosis and health care. Such applications are extremely challenging for Raman-based techniques due to high demands in sensitivity, specificity, throughput and lateral resolution. CRS techniques are expected to overcome some of the challenges in the future once the instrumentation is less complex. For this reason, CRS laser sources were presented in more details. Spontaneous Raman instrumentation already matured to a level that can be translated to hospitals soon. Important links that are still under development and that were not covered here are automated algorithms for data processing and classification. The society CLIRSPEC, and the networks CLIRSPEC and Raman4clinics were launched to foster collaboration between groups, elaborate standard operating procedures, and design experiments for proper validation. Most of the authors of this topical issue are involved in these initiatives and the interested research community is welcome to join this exciting topic.

Acknowledgements

Financial supports of the EU, ESF, EFRE, the "Thüringer Kultusministerium", the "Thüringer Aufbaubank", the Federal Ministry of Education and Research, Germany (BMBF), the German Science Foundation (DFG), the Fonds der Chemischen Industrie and the Carl-Zeiss Foundation are greatly acknowledged.

Notes and references

1. C. Krafft and J. Popp, *Anal. Bioanal. Chem.*, 2015, 407, 699-717.
2. I. W. Schie, C. Krafft and J. Popp, *Analyst*, 2015, 140, 3897-3909.
3. M. Diem, A. Mazur, K. Lenau, J. Schubert, B. Bird, M. Miljkovic, C. Krafft and J. Popp, *Journal of biophotonics*, 2013, 6, 855-886.
4. N. Vogler, S. Heuke, T. W. Bocklitz, M. Schmitt and J. Popp, *Annual Review of Analytical Chemistry*, 2015, 8, 359-387.
5. P. R. Carey, *Journal of Biological Chemistry*, 1999, 274, 26625-26628.
6. J. L. Abraham and E. S. Etz, *Science*, 1979, 206, 3.
7. E. S. Etz and J. J. Blaha, *National Beuro of Standards* 1980, 1, 44.
8. J. F. Brennan, Y. Wang, R. R. Dasari and M. S. Feld, *Appl. Spectrosc.*, 1997, 51, 201-208.
9. P. Vandenabeele, *Practical Raman Spectroscopy: An Introduction*, Wiley, Hoboken, 2013.
10. McCreery, http://www.chem.ualberta.ca/~mccreery/ramanmaterials.html.
11. S. Hanf, T. Bogozi, R. Keiner, T. Frosch and J. Popp, *Anal. Chem.*, 2015, 87, 982-988.
12. M. Mazilu, A. C. De Luca, A. Riches, C. S. Herrington and K. Dholakia, *Optics Express*, 2010, 18, 11382-11395.
13. S. Dochow, N. Bergner, C. Matthäus, B. Praveen, P. C. Ashok, M. Mazilu, C. Krafft, K. Dholakia and J. Popp, *Biomedical Spectroscopy and Imaging*, 2012, 1, 383-389.
14. D. Wei, S. Chen and Q. Liu, *Appl. Spectrosc. Rev.*, 2015, 50, 387-406.
15. S. Choi, G. B. Jung, K. S. Kim, G. J. Lee and H. K. Park, *J. Nanosci. Nanotechnol.*, 2014, 14, 71-97.
16. T. Schmid, L. Opilik, C. Blum and R. Zenobi, *Angew. Chem.-Int. Edit.*, 2013, 52, 5940-5954.
17. D. A. Schmidt, I. Kopf and E. Brundermann, *Laser Photon. Rev.*, 2012, 6, 296-332.
18. C. Julien and C. Hirlimann, *J. Raman Spectrosc.*, 1980, 9, 62-66.
19. D. A. Carter, W. R. Thompson, C. E. Taylor and J. E. Pemberton, *Appl. Spectrosc.*, 1995, 49, 1561-1576.
20. D. E. Battey, J. B. Slater, R. Wludyka, H. Owen, D. M. Pallister and M. D. Morris, *Appl. Spectrosc.*, 1993, 47, 1913-1919.
21. H. Owen, *J. Chem. Educ.*, 2007, 84, 61-66.
22. P. J. Larkin, M. Dabros, B. Sarsfield, E. Chan, J. T. Carriere and B. C. Smith, *Appl. Spectrosc.*, 2014, 68, 758-776.
23. T. Dieing and O. Hollricher, *Vib. Spectrosc.*, 2008, 48, 22-27.
24. J. Kostamovaara, J. Tenhunen, M. Kogler, I. Nissinen, J. Nissinen and P. Keranen, *Optics Express*, 2013, 21, 31632-31645.
25. C. L. Evans, E. O. Potma, M. Puoris'haag, D. Côté, C. P. Lin and X. S. Xie, *PNAS*, 2005, 102, 16807-16812.
26. B. G. Saar, C. W. Freudiger, J. Reichman, C. M. Stanley, G. R. Holtom and X. S. Xie, *Science*, 2010, 330, 1368-1370.
27. A. Zumbusch, G. R. Holtom and X. S. Xie, *Physical Review Letters*, 1999, 82, 4142-4145.
28. C. W. Freudiger, W. Min, B. G. Saar, S. Lu, G. R. Holtom, C. He, J. C. Tsai, J. X. Kang and X. S. Xie, *Science*, 2008, 322, 1857-1861.
29. E. Ploetz, S. Laimgruber, S. Berner, W. Zinth and P. Gilch, *Appl. Phys. B*, 2007, 87, 389-393.
30. B. R. Bachler, M. E. Fermann and J. P. Ogilvie, *Optics Express*, 2012, 20, 835.
31. C. W. Freudiger, M. B. J. Roeffaers, X. Zhang, B. G. Saar, W. Min and X. S. Xie, *J. Phys. Chem. B*, 2011, 115, 5574-5581.
32. E. Molotokaite, V. Kumar, C. Manzoni, D. Polli, G. Cerullo and M. Marangoni, *J. Raman Spectrosc.*, 2013, 44, 1385-1392.
33. T. Gottschall, T. Meyer, M. Baumgartl, C. Jauregui, M. Schmitt, J. Popp, J. Limpert and A. Tünnermann, *Laser Photon. Rev.*, 2015, DOI: 10.1002/lpor.201500023, n/a-n/a.
34. D. Fu, G. Holtom, C. Freudiger, X. Zhang and X. S. Xie, *The Journal of Physical Chemistry B*, 2013, 117, 4634-4640.
35. D. Fu and X. S. Xie, *Anal. Chem.*, 2014, 86, 4115-4119.
36. F. Masia, A. Glen, P. Stephens, P. Borri and W. Langbein, *Anal. Chem.*, 2013, 85, 10820-10828.
37. C.-Y. Lin, J. L. Suhalim, C. L. Nien, M. D. Miljković, M. Diem, J. V. Jester and E. O. Potma, *Journal of Biomedical Optics*, 2011, 16, 021104-021104-021109.
38. E. Belanger, J. Crepeau, S. Laffray, R. Vallee, Y. De Koninck and D. Cote, *Journal of biomedical optics*, 2012, 17, 021107-021107.
39. C.-S. Liao, M. N. Slipchenko, P. Wang, J. Li, S.-Y. Lee, R. A. Oglesbee and J.-X. Cheng, *Light Sci Appl*, 2015, 4, e265.
40. C. H. C. Jr, Y. J. Lee, J. M. Heddleston, C. M. Hartshorn, A. R. H. Walker, J. N. Rich, J. D. Lathia and M. T. Cicerone, *Nat Photon*, 2014, 8, 627-634.
41. N. Dudovich, D. Oron and Y. Silberberg, *Nature*, 2002, 418, 512-514.
42. H. Frostig, O. Katz, A. Natan and Y. Silberberg, *Optics Letters*, 2011, 36, 1248-1250.
43. S. Kumar, T. Kamali, J. M. Levitte, O. Katz, B. Hermann, R. Werkmeister, B. Považay, W. Drexler, A. Unterhuber and Y. Silberberg, *Optics Express*, 2015, 23, 13082-13098.
44. J. Rehbinder, L. Brückner, A. Wipfler, T. Buckup and M. Motzkus, *Optics Express*, 2014, 22, 28790-28797.
45. A. Wipfler, T. Buckup and M. Motzkus, *Applied Physics Letters*, 2012, 100, 071102.
46. A. Wipfler, J. Rehbinder, T. Buckup and M. Motzkus, *Optics Letters*, 2012, 37, 4239-4241.
47. J. P. Ogilvie, E. Beaurepaire, A. Alexandrou and M. Joffre, *Optics Letters*, 2006, 31, 480-482.
48. T. Ideguchi, S. Holzner, B. Bernhardt, G. Guelachvili, N. Picqué and T. W. Hänsch, *Nature*, 2013, 502, 355-358.
49. K. König, H. Liang, M. W. Berns and B. J. Tromberg, *Nature*, 1995, 377, 20-21.
50. K. König, P. T. C. So, W. W. Mantulin and E. Gratton, *Optics Letters*, 1997, 22, 135-136.
51. Y. Fu, H. Wang, R. Shi and J.-X. Cheng, *Optics Express*, 2006, 14, 3942-3951.
52. H. Wang, Y. Fu and J.-X. Cheng, *J. Opt. Soc. Am. B*, 2007, 24, 544-552.
53. A. Hopt and E. Neher, *Biophysical Journal*, 2001, 80, 2029-2036.
54. K. König, T. W. Becker, P. Fischer, I. Riemann and K. J. Halbhuber, *Optics Letters*, 1999, 24, 113-115.
55. J.-X. Cheng and X. S. Xie, *The Journal of Physical Chemistry B*, 2004, 108, 827-840.
56. L. Wei, F. Hu, Y. Shen, Z. Chen, Y. Yu, C.-C. Lin, M. C. Wang and W. Min, *Nat Meth*, 2014, 11, 410-412.
57. T. Meyer, M. Chemnitz, M. Baumgartl, T. Gottschall, T. Pascher, C. Matthäus, B. F. M. Romeike, B. R. Brehm, J. Limpert, A. Tünnermann, M. Schmitt, B. Dietzek and J. Popp, *Anal. Chem.*, 2013, 85, 6703-6715.

58. K. Ibata, S. Takimoto, T. Morisaku, A. Miyawaki and M. Yasui, *Biophysical Journal*, 2011, 101, 2277-2283.
59. E. O. Potma, W. P. d. Boeij, P. J. M. v. Haastert and D. A. Wiersma, *Proceedings of the National Academy of Sciences*, 2001, 98, 1577-1582.
60. Y.-C. Yu, Y. Sohma, S. Takimoto, T. Miyauchi and M. Yasui, *Sci. Rep.*, 2013, 3.
61. L. Wei, Y. Shen, F. Xu, F. Hu, J. K. Harrington, K. L. Targoff and W. Min, *ACS Chem. Biol.*, 2015, 10, 901-908.
62. S. Hong, T. Chen, Y. Zhu, A. Li, Y. Huang and X. Chen, *Angew. Chem.*, 2014, 126, 5937-5941.
63. Z. Chen, D. W. Paley, L. Wei, A. L. Weisman, R. A. Friesner, C. Nuckolls and W. Min, *J. Am. Chem. Soc.*, 2014, 136, 8027-8033.
64. L. Wei, Y. Yu, Y. Shen, M. C. Wang and W. Min, *Proceedings of the National Academy of Sciences*, 2013, 110, 11226-11231.
65. X. Zhang, M. B. J. Roeffaers, S. Basu, J. R. Daniele, D. Fu, C. W. Freudiger, G. R. Holtom and X. S. Xie, *ChemPhysChem*, 2012, 13, 1054-1059.
66. M. D. Duncan, J. Reintjes and T. J. Manuccia, *Optics letters*, 1982, 7, 350-352.
67. D. J. Jones, E. O. Potma, J.-x. Cheng, B. Burfeindt, Y. Pang, J. Ye and X. S. Xie, *Review of Scientific Instruments*, 2002, 73, 2843-2848.
68. J.-x. Cheng, A. Volkmer, L. D. Book and X. S. Xie, *The Journal of Physical Chemistry B*, 2001, 105, 1277-1280.
69. P. Nandakumar, A. Kovalev and A. Volkmer, *New J. Phys.*, 2009, 11, 033026.
70. E. O. Potma, W. P. d. Boeij and D. A. Wiersma, *J. Opt. Soc. Am. B, JOSAB*, 2000, 17, 1678-1684.
71. E. Büttner, S. Carrasco, C. L. Evans, F. S. Ganikhanov, J. G. Herbst, D. Kopf, I. Rimke and S. Xie, 2007.
72. F. Ganikhanov, S. Carrasco, X. Sunney Xie, M. Katz, W. Seitz and D. Kopf, *Optics letters*, 2006, 31, 1292-1294.
73. S. Brustlein, P. Ferrand, N. Walther, S. Brasselet, C. Billaudeau, D. Marguet and H. Rigneault, *Journal of biomedical optics*, 2011, 16, 021106-021106-021110.
74. K. Kieu, B. G. Saar, G. R. Holtom, X. S. Xie and F. W. Wise, *Optics letters*, 2009, 34, 2051-2053.
75. I. Rimke, G. Hehl, M. Beutler, P. Volz, A. Volkmer and E. Büttner, 2014.
76. H. Kano and H.-o. Hamaguchi, *Optics letters*, 2003, 28, 2360-2362.
77. T. W. Kee and M. T. Cicerone, *Optics letters*, 2004, 29, 2701-2703.
78. E. R. Andresen, V. Birkedal, J. Thøgersen and S. R. Keiding, *Optics letters*, 2006, 31, 1328-1330.
79. A. A. Ivanov, A. A. Podshivalov and A. M. Zheltikov, *Optics letters*, 2006, 31, 3318-3320.
80. S. Lefrancois, D. Fu, G. R. Holtom, L. Kong, W. J. Wadsworth, P. Schneider, R. Herda, A. Zach, X. Sunney Xie and F. W. Wise, *Optics letters*, 2012, 37, 1652-1654.
81. E. S. Lamb, S. Lefrancois, M. Ji, W. J. Wadsworth, X. Sunney Xie and F. W. Wise, *Optics letters*, 2013, 38, 4154.
82. H. Kano and H.-o. Hamaguchi, *Anal. Chem.*, 2007, 79, 8967-8973.
83. H. Kano and H.-o. Hamaguchi, *Optics Express*, 2006, 14, 2798-2804.
84. H. Kano and H.-o. Hamaguchi, *Optics Express*, 2005, 13, 1322-1327.
85. H. Kano and H.-o. Hamaguchi, *Applied Physics Letters*, 2004, 85, 4298-4300.
86. E. R. Andresen, H. N. Paulsen, V. Birkedal, J. Thøgersen and S. R. Keiding, *J. Opt. Soc. Am. B*, 2005, 22, 1934-1938.
87. V. Yakovlev and G. I. Petrov, *Optics Express*, 2005, 13, 1299-1306.
88. P. Groß, L. Kleinschmidt, S. Beer, C. Cleff and C. Fallnich, *Appl. Phys. B*, 2010, 101, 167-172.
89. S. Saint-Jalm, P. Berto, L. Jullien, E. R. Andresen and H. Rigneault, *J. Raman Spectrosc.*, 2014, 45, 515-520.
90. Y.-H. Zhai, C. Goulart, J. E. Sharping, H. Wei, S. Chen, W. Tong, M. N. Slipchenko, D. Zhang and J.-X. Cheng, *Applied Physics Letters*, 2011, 98, 191106.
91. M. Okuno, H. Kano, P. Leproux, V. Couderc and H.-o. Hamaguchi, *Optics letters*, 2008, 33, 923.
92. H. Mikami, M. Shiozawa, M. Shirai and K. Watanabe, *Optics Express*, 2015, 23, 2872.
93. S. Begin, B. Burgoyne, V. Mercier, A. Villeneuve, R. Vallee and D. Cote, *Biomedical optics express*, 2011, 2, 1296-1306.
94. H. Kano and H.-o. Hamaguchi, *Applied Physics Letters*, 2005, 86, 121113.
95. T. Gottschall, M. Baumgartl, A. Sagnier, J. Rothhardt, C. Jauregui, J. Limpert and A. Tünnermann, *Optics Express*, 2012, 20, 12004.
96. A. F. Pegoraro, A. Ridsdale, D. J. Moffatt, J. P. Pezacki, B. K. Thomas, L. Fu, L. Dong, M. E. Fermann and A. Stolow, *Optics Express*, 2009, 17, 20700-20706.
97. T. Hellerer, A. M. K. Enejder and A. Zumbusch, *Applied Physics Letters*, 2004, 85, 25-27.
98. E. R. Andresen, P. Berto and H. Rigneault, *Optics letters*, 2011, 36, 2387.
99. G. Krauss, T. Hanke, A. Sell, D. Träutlein, A. Leitenstorfer, R. Selm, M. Winterhalder and A. Zumbusch, *Optics letters*, 2009, 34, 2847-2849.
100. R. Galli, O. Uckermann, M. J. Winterhalder, K. H. Sitoci-Ficici, K. D. Geiger, E. Koch, G. Schackert, A. Zumbusch, G. Steiner and M. Kirsch, *Anal. Chem.*, 2012, 84, 8707-8714.
101. M. Chemnitz, M. Baumgartl, T. Meyer, C. Jauregui, B. Dietzek, J. Popp, J. Limpert and A. Tünnermann, *Optics Express*, 2012, 20, 26583-26595.
102. M. Baumgartl, T. Gottschall, J. Abreu-Afonso, A. Díez, T. Meyer, B. Dietzek, M. Rothhardt, J. Popp, J. Limpert and A. Tünnermann, *Optics Express*, 2012, 20, 21010-21018.
103. T. Gottschall, T. Meyer, M. Baumgartl, B. Dietzek, J. Popp, J. Limpert and A. Tünnermann, *Optics Express*, 2014, 22, 21921-21928.
104. V. V. Yakovlev, G. I. Petrov, G. D. Noojin, C. Harbert, M. Denton and R. Thomas, *Journal of biophotonics*, 2010, 3, 653-659.
105. Z. Meng, G. I. Petrov and V. V. Yakovlev, *Appl. Phys. B*, 2013, 112, 99-103.
106. C.-R. Hu, M. N. Slipchenko, P. Wang, P. Wang, J. D. Lin, G. Simpson, B. Hu and J.-X. Cheng, *Optics letters*, 2013, 38, 1479.
107. K. Wang, C. W. Freudiger, J. H. Lee, B. G. Saar, X. S. Xie and C. Xu, *Optics Express*, 2010, 18, 24019-24024.
108. K. Wang, D. Zhang, K. Charan, M. N. Slipchenko, P. Wang, C. Xu and J.-X. Cheng, *Journal of biophotonics*, 2013, 6, 815-820.
109. S. Karpf, M. Eibl, W. Wieser, T. Klein and R. Huber, *Nat Commun*, 2015, 6.
110. C. Jüngst, M. J. Winterhalder and A. Zumbusch, *Journal of biophotonics*, 2011, 4, 435-441.
111. Samir F. El-Mashtoly, D. Niedieker, D. Petersen, Sascha D. Krauss, E. Freier, A. Maghnouj, A. Mosig, S. Hahn, C. Kötting and K. Gerwert, *Biophysical Journal*, 2014, 106, 1910-1920.

112.A. F. Pegoraro, A. Stolow, A. Ridsdale, D. J. Moffatt, J. P. Pezacki and Y. Jia, *Biophotonics*, 2009.
113.N. Corporation, 2012.
114.O. A. Inc., 2012.
115.R. Selm, M. Winterhalder, A. Zumbusch, G. n. Krauss, T. Hanke, A. Sell and A. Leitenstorfer, *Optics letters*, 2010, 35, 3282-3284.
116.Y. Fu, T. B. Huff, H.-W. Wang, H. Wang and J.-X. Cheng, *Optics Express*, 2008, 16, 19396-19409.
117.T. Meyer, M. Schmitt, B. Dietzek and J. Popp, *JOURNAL OF BIOPHOTONICS*, 2013, 6, 887-904.
118.H. P. K.K., 2006.
119.A. Downes, R. Mouras and A. Elfick, *J. Raman Spectrosc.*, 2009, 40, 757-762.
120.D. Zhang, M. N. Slipchenko and J.-X. Cheng, *J. Phys. Chem. Lett.*, 2011, 2, 1248-1253.
121.K. Nose, Y. Ozeki, T. Kishi, K. Sumimura, N. Nishizawa, K. Fukui, Y. Kanematsu and K. Itoh, *Optics Express*, 2012, 20, 13958-13965.
122.C. W. Freudiger, W. Yang, G. R. Holtom, N. Peyghambarian, X. S. Xie and K. Q. Kieu, *Nat Photon*, 2014, 8, 153-159.
123.M. N. Slipchenko, R. A. Oglesbee, D. Zhang, W. Wu and J.-X. Cheng, *Journal of biophotonics*, 2012, 5, 801-807.
124.K. Seto, T. Tsukada, Y. Okuda, E. Tokunaga and T. Kobayashi, *Journal of the Optical Society of America A*, 2015, 32, 809.
125.W. Rock, M. Bonn and S. H. Parekh, *Optics Express*, 2013, 21, 15113.
126.I. W. Schie and T. Huser, *Appl. Spectrosc.*, 2013, 67, 813-828.
127.D. A. Long, *New York*, 1977, 1-12.
128.R. Lord and N.-T. Yu, *Journal of molecular biology*, 1970, 50, 509-524.
129.H. W. Siesler and K. Holland-Moritz, *Infrared and Raman spectroscopy of polymers*, M. Dekker, 1980.
130.M. Minsky, Google Patents, 1957.
131.J. B. Pawley, in *Handbook of biological confocal microscopy*, Springer, 2006, pp. 20-42.
132.G. Puppels, F. De Mul, C. Otto, J. Greve, M. Robert-Nicoud, D. Arndt-Jovin and T. Jovin, 1990.
133.G. Puppels, W. Colier, J. Olminkhof, C. Otto, F. d. Mul and J. Greve, *J. Raman Spectrosc.*, 1991, 22, 217-225.
134.R. Tabaksblat, R. J. Meier and B. J. Kip, *Appl. Spectrosc.*, 1992, 46, 60-68.
135.T. Wilson, *Academic Press: London, etc*, 1990, 426, 1-64.
136.C. De Grauw, N. Sijtsema, C. Otto and J. Greve, *Journal of Microscopy*, 1997, 188, 273-279.
137.N. J. Everall, *Analyst*, 2010, 135, 2512-2522.
138.N. Everall, *J. Raman Spectrosc.*, 2014, 45, 133-138.
139.A. Ashkin, *Physical review letters*, 1970, 24, 156.
140.M. C. Williams, *Biophysics Textbook Online: http://www. biophysics. org/btol*, 2002.
141.A. Ashkin, *Proceedings of the National Academy of Sciences*, 1997, 94, 4853-4860.
142.D. G. Grier, *Nature*, 2003, 424, 810-816.
143.M. Capitanio and F. S. Pavone, *Biophysical Journal*, 2013, 105, 1293-1303.
144.H. Misawa, K. Sasaki, M. Koshioka, N. Kitamura and H. Masuhara, *Applied Physics Letters*, 1992, 60, 310-312.
145.R. Liu, D. S. Taylor, D. L. Matthews and J. W. Chan, *Appl. Spectrosc.*, 2010, 64, 1308-1310.
146.P. Zhang, L. Kong, P. Setlow and Y.-q. Li, *Optics letters*, 2010, 35, 3321-3323.
147.L. Kong and J. Chan, *Anal. Chem.*, 2014, 86, 6604-6609.
148.J. W. Chan, *Journal of biophotonics*, 2013, 6, 36-48.
149.R. D. Snook, T. J. Harvey, E. C. Faria and P. Gardner, *Integrative Biology*, 2009, 1, 43-52.
150.L. Kong, P. Zhang, J. Yu, P. Setlow and Y.-q. Li, *Applied Physics Letters*, 2011, 98, 213703.
151.M. Delhaye and P. Dhamelincourt, *J. Raman Spectrosc.*, 1975, 3, 33-43.
152.M. Okuno and H.-o. Hamaguchi, *Optics letters*, 2010, 35, 4096-4098.
153.L. Kong, P. Zhang, P. Setlow and Y.-q. Li, *Journal of biomedical optics*, 2011, 16, 120503-1205033.
154.J. Qi and W.-C. Shih, *Optics letters*, 2012, 37, 1289-1291.
155.J. Qi, J. Li and W.-C. Shih, *Biomedical optics express*, 2013, 4, 2376-2382.
156.D. K. Veirs, J. W. Ager, E. T. Loucks and G. M. Rosenblatt, *Applied optics*, 1990, 29, 4969-4980.
157.M. Ivanda and K. Furić, *Applied optics*, 1992, 31, 6371-6375.
158.C. A. Drumm and M. D. Morris, *Appl. Spectrosc.*, 1995, 49, 1331-1337.
159.K. A. Christensen and M. D. Morris, *Appl. Spectrosc.*, 1998, 52, 1145-1147.
160.C. De Grauw, C. Otto and J. Greve, *Appl. Spectrosc.*, 1997, 51, 1607-1612.
161.K. Hamada, K. Fujita, N. I. Smith, M. Kobayashi, Y. Inouye and S. Kawata, *Journal of biomedical optics*, 2008, 13, 044027-044027-044024.
162.Y. Oshima, H. Sato, H. Kajiura-Kobayashi, T. Kimura, K. Naruse and S. Nonaka, *Optics express*, 2012, 20, 16195-16204.
163.J. Qi and W.-C. Shih, *Applied optics*, 2014, 53, 2881-2885.
164.I. W. Schie, L. Alber, A. L. Gryshuk and J. W. Chan, *Analyst*, 2014, 139, 2726-2733.
165.G. Turrell and J. Corset, *Raman microscopy: developments and applications*, Academic Press, 1996.
166.P. J. Treado, I. W. Levin and E. N. Lewis, *Appl. Spectrosc.*, 1992, 46, 1211-1216.
167.M. D. Schaeberle, H. R. Morris, J. F. T. II and P. J. Treado, *Anal. Chem.*, 1999, 71, 175A-181A.
168.S. Schlücker, M. D. Schaeberle, S. W. Huffman and I. W. Levin, *Anal. Chem.*, 2003, 75, 4312-4318.
169.R. W. Havener, S.-Y. Ju, L. Brown, Z. Wang, M. Wojcik, C. S. Ruiz-Vargas and J. Park, *ACS nano*, 2011, 6, 373-380.
170.A. Tripathi, E. D. Emmons, P. G. Wilcox, J. A. Guicheteau, D. K. Emge, S. D. Christesen and A. W. Fountain III, *Appl. Spectrosc.*, 2011, 65, 611-619.
171.A. Volkmer, J.-X. Cheng and X. S. Xie, *Physical review letters*, 2001, 87, 023901.
172.I. W. Schie, T. Weeks, G. P. McNerney, S. Fore, J. K. Sampson, S. Wachsmann-Hogiu, J. C. Rutledge and T. Huser, *Optics express*, 2008, 16, 2168-2175.
173.M. Hashimoto, T. Araki and S. Kawata, *Optics letters*, 2000, 25, 1768-1770.
174.E. Fällman and O. Axner, *Applied optics*, 1997, 36, 2107-2113.
175.J.-X. Cheng, Y. K. Jia, G. Zheng and X. S. Xie, *Biophysical Journal*, 2002, 83, 502-509.
176.T. Minamikawa, M. Hashimoto, K. Fujita, S. Kawata and T. Araki, *Optics express*, 2009, 17, 9526-9536.
177.C. Heinrich, S. Bernet and M. Ritsch-Marte, *Applied Physics Letters*, 2004, 84, 816-818.
178.C. Heinrich, C. Meusburger, S. Bernet and M. Ritsch-Marte, *J. Raman Spectrosc.*, 2006, 37, 675-679.
179.C. Heinrich, A. Hofer, A. Ritsch, C. Ciardi, S. Bernet and M. Ritsch-Marte, *Optics express*, 2008, 16, 2699-2708.

180.I. Toytman, D. Simanovskii and D. Palanker, *Optics express*, 2009, 17, 7339-7347.
181.S. Heuke, J. Zheng, D. Akimov, R. Heintzmann, M. Schmitt and J. Popp, *Sci. Rep.*, 2015, 5.
182.R. S. Lim, J. L. Suhalim, S. Miyazaki-Anzai, M. Miyazaki, M. Levi, E. O. Potma and B. J. Tromberg, *J. Lipid Res.*, 2011, 52, 2177-2186.
183.Jeffrey L. Suhalim, C.-Y. Chung, Magnus B. Lilledahl, Ryan S. Lim, M. Levi, Bruce J. Tromberg and Eric O. Potma, *Biophysical Journal*, 2012, 102, 1988-1995.
184.D. Fu, Y. Yu, A. Folick, E. Currie, R. V. Farese, T.-H. Tsai, X. S. Xie and M. C. Wang, *J. Am. Chem. Soc.*, 2014, 136, 8820-8828.
185.M. Müller and J. M. Schins, *The Journal of Physical Chemistry B*, 2002, 106, 3715-3723.
186.C. Pohling, T. Buckup, A. Pagenstecher and M. Motzkus, *Biomedical Optics Express*, 2011, 2, 2110-2116.
187.S. H. Parekh, Y. J. Lee, K. A. Aamer and M. T. Cicerone, *Biophysical Journal*, 2010, 99, 2695-2704.
188.H. Kano and H. Hamaguchi, *Appl. Phys. B*, 2005, 80, 243-246.
189.H. Kano, *J. Raman Spectrosc.*, 2008, 39, 1649-1652.
190.H. A. Rinia, K. N. J. Burger, M. Bonn and M. Müller, *Biophysical Journal*, 2008, 95, 4908-4914.
191.M. Bonn, M. Müller, H. A. Rinia and K. N. J. Burger, *J. Raman Spectrosc.*, 2009, 40, 763-769.
192.J. Y. Lee, S.-H. Kim, D. W. Moon and E. S. Lee, *Optics Express*, 2009, 17, 22281.
193.N. Billecke, G. Rago, M. Bosma, G. Eijkel, A. Gemmink, P. Leproux, G. Huss, P. Schrauwen, M. K. C. Hesselink, M. Bonn and S. H. Parekh, *Histochem Cell Biol*, 2013, 141, 263-273.
194.C. H. Camp Jr and M. T. Cicerone, *Nat Photon*, 2015, 9, 295-305.
195.E. M. Vartiainen, H. A. Rinia, M. Müller and M. Bonn, *Optics Express*, 2006, 14, 3622-3630.
196.M. T. Cicerone, K. A. Aamer, Y. J. Lee and E. Vartiainen, *J. Raman Spectrosc.*, 2012, 43, 637-643.
197.J. P. R. Day, K. F. Domke, G. Rago, H. Kano, H.-o. Hamaguchi, E. M. Vartiainen and M. Bonn, *The Journal of Physical Chemistry B*, 2011, 115, 7713-7725.
198.J. M. Levitt, O. Katz and Y. Silberberg, *Journal of Modern Optics*, 2014, 61, 872-876.
199.W. Langbein, I. Rocha-Mendoza and P. Borri, *J. Raman Spectrosc.*, 2009, 40, 800-808.
200.A. F. Pegoraro, A. Ridsdale, D. J. Moffatt, Y. Jia, J. P. Pezacki and A. Stolow, *Optics Express*, 2009, 17, 2984-2996.
201.I. Rocha-Mendoza, W. Langbein and P. Borri, *Applied Physics Letters*, 2008, 93, 201103.
202.C. Krafft, T. Knetschke, R. H. Funk and R. Salzer, *Anal. Chem.*, 2006, 78, 4424-4429.
203.U. Neugebauer, J. H. Clement, T. Bocklitz, C. Krafft and J. Popp, *J Biophotonics*, 2010, 3, 579-587.
204.C. Matthäus, C. Krafft, B. Dietzek, B. R. Brehm, S. Lorkowski and J. Popp, *Anal. Chem.*, 2012, 84, 8549-8556.
205.C. Stiebing, C. Matthäus, C. Krafft, A. A. Keller, K. Weber, S. Lorkowski and J. Popp, *Anal Bioanal Chem*, 2014, 406, 7037-7046.
206.D. Zhang, P. Wang, M. N. Slipchenko and J.-X. Cheng, *Acc. Chem. Res.*, 2014, 47, 2282-2290.
207.S. Yue, J. Li, S.-Y. Lee, Hyeon J. Lee, T. Shao, B. Song, L. Cheng, Timothy A. Masterson, X. Liu, Timothy L. Ratliff and J.-X. Cheng, *Cell Metabolism*, 2014, 19, 393-406.
208.I. W. Schie, L. Nolte, T. L. Pedersen, Z. Smith, J. Wu, I. Yahiatene, J. W. Newman and T. Huser, *Analyst*, 2013, 138, 6662-6670.
209.M. N. Slipchenko, T. T. Le, H. T. Chen and J. X. Cheng, *Journal of Physical Chemistry B*, 2009, 113, 7681-7686.
210.C. Xie, M. A. Dinno and Y.-q. Li, *Optics letters*, 2002, 27, 249-251.
211.C. Xie and Y.-q. Li, *Journal of Applied Physics*, 2003, 93, 2982-2986.
212.J. Chan, A. Esposito, C. Talley, C. Hollars, S. Lane and T. Huser, *Anal. Chem.*, 2004, 76, 599-603.
213.C. Xie, J. Mace, M. Dinno, Y. Li, W. Tang, R. Newton and P. Gemperline, *Anal. Chem.*, 2005, 77, 4390-4397.
214.J. W. Chan, D. S. Taylor, S. M. Lane, T. Zwerdling, J. Tuscano and T. Huser, *Anal. Chem.*, 2008, 80, 2180-2187.
215.J. W. Chan, D. S. Taylor and D. L. Thompson, *Biopolymers*, 2009, 91, 132-139.
216.T. J. Moritz, D. S. Taylor, D. M. Krol, J. Fritch and J. W. Chan, *Biomedical optics express*, 2010, 1, 1138-1147.
217.E. Brauchle, S. Thude, S. Y. Brucker and K. Schenke-Layland, *Sci. Rep.*, 2014, 4.
218.H. Tang, H. Yao, G. Wang, Y. Wang, Y.-q. Li and M. Feng, *Optics express*, 2007, 15, 12708-12716.
219.S. Fore, J. Chan, D. Taylor and T. Huser, *Journal of Optics*, 2011, 13, 044021.
220.K. Ramser, J. Enger, M. Goksör, D. Hanstorp, K. Logg and M. Käll, *Lab on a Chip*, 2005, 5, 431-436.
221.A. Y. Lau, L. P. Lee and J. W. Chan, *Lab on a Chip*, 2008, 8, 1116-1120.
222.S. Dochow, C. Krafft, U. Neugebauer, T. Bocklitz, T. Henkel, G. Mayer, J. Albert and J. Popp, *Lab on a Chip*, 2011, 11, 1484-1490.
223.S. Dochow, C. Beleites, T. Henkel, G. Mayer, J. Albert, J. Clement, C. Krafft and J. Popp, *Anal. Bioanal. Chem.*, 2013, 405, 2743-2746.
224.C. Krafft, B. Belay, N. Bergner, B. F. Romeike, R. Reichart, R. Kalff and J. Popp, *Analyst*, 2012, 137, 5533-5537.
225.N. Bergner, A. Medyukhina, K. D. Geiger, M. Kirsch, G. Schackert, C. Krafft and J. Popp, *Anal. Bioanal. Chem.*, 2013, 405, 8719-8728.
226.K. Kong, C. J. Rowlands, S. Varma, W. Perkins, I. H. Leach, A. A. Koloydenko, H. C. Williams and I. Notingher, *PNAS*, 2013, 110, 15189-15194.
227.M. Kirsch, G. Schackert, R. Salzer and C. Krafft, *Anal Bioanal Chem*, 2010, 398, 1707-1713.
228.S. Dochow, D. Ma, I. Latka, T. Bocklitz, B. Hartl, J. Bec, H. Fatakdawala, E. Marple, K. Urmey, S. Wachsmann-Hogiu, M. Schmitt, L. Marcu and J. Popp, *Anal Bioanal Chem*, 2015, DOI: DOI 10.1007/s00216-015-8800-5.
229.E. Schmalzlin, B. Moralejo, M. Rutowska, A. Monreal-Ibero, C. Sandin, N. Tarcea, J. Popp and M. M. Roth, *Sensors*, 2014, 14, 21968-21980.
230.A. Lukic, S. Dochow, O. Chernavskaia, I. Latka, C. Matthäus, A. Schwuchow, M. Schmitt and J. Popp, *J. Biophotonics*, 2015, DOI: 10.1002/jbio.201500010.
231.C. Zavaleta, A. de la Zerda, Z. Liu, S. Keren, Z. Cheng, M. Schipper, X. Chen, H. Dai and S. S. Gambhir, *Nano Lett*, 2008, 8, 2800-2805.
232.S. E. Bohndiek, A. Wagadarikar, C. L. Zavaleta, D. Van de Sompel, E. Garai, J. V. Jokerst, S. Yazdanfar and S. S. Gambhir, *PNAS*, 2013, 110, 12408-12413.
233.W. Gellermann, I. V. Ermakov, R. W. McClane and P. S. Bernstein, *Optics Letters*, 2002, 27, 833-835.
234.M. B. Ji, D. A. Orringer, C. W. Freudiger, S. Ramkissoon, X. H. Liu, D. Lau, A. J. Golby, I. Norton, M. Hayashi, N. Y. R. Agar, G. S.

Young, C. Spino, S. Santagata, S. Camelo-Piragua, K. L. Ligon, O. Sagher and X. S. Xie, *Sci. Transl. Med.*, 2013, 5, 201ra119.

235. G. Bergner, C. R. Albert, M. Schiller, G. Bringmann, T. Schirmeister, B. Dietzek, S. Niebling, S. Schlücker and J. Popp, *Analyst*, 2011, 136, 3686-3693.

236. N. L. Garrett, A. Lalatsa, I. Uchegbu, A. Schätzlein and J. Moger, *Journal of Biophotonics*, 2012, 5, 458-468.

237. C. M. Hartshorn, Y. J. Lee, C. H. Camp, Z. Liu, J. Heddleston, N. Canfield, T. A. Rhodes, A. R. Hight Walker, P. J. Marsac and M. T. Cicerone, *Anal. Chem.*, 2013, 85, 8102-8111.

238. A. Fussell, E. Garbacik, H. Offerhaus, P. Kleinebudde and C. Strachan, *European Journal of Pharmaceutics and Biopharmaceutics*, 2013, 85, 1141-1147.

239. P. C. Christophersen, D. Birch, J. Saarinen, A. Isomäki, H. M. Nielsen, M. Yang, C. J. Strachan and H. Mu, *Journal of Controlled Release*, 2015, 197, 111-120.

240. B. G. Saar, L. R. Contreras-Rojas, X. S. Xie and R. H. Guy, *Mol. Pharmaceutics*, 2011, 8, 969-975.

241. G. P. S. Smith, C. M. McGoverin, S. J. Fraser and K. C. Gordon, *Advanced Drug Delivery Reviews*, DOI: 10.1016/j.addr.2015.01.005.

242. R. M. Goodhead, J. Moger, T. S. Galloway and C. R. Tyler, *Nanotoxicology*, 2015, 0, 1-12.

243. N. A. Belsey, N. L. Garrett, L. R. Contreras-Rojas, A. J. Pickup-Gerlaugh, G. J. Price, J. Moger and R. H. Guy, *Journal of Controlled Release*, 2014, 174, 37-42.

244. C. W. Freudiger, R. Pfannl, D. A. Orringer, B. G. Saar, M. Ji, Q. Zeng, L. Ottoboni, W. Ying, C. Waeber, J. R. Sims, P. L. D. Jager, O. Sagher, M. A. Philbert, X. Xu, S. Kesari, X. S. Xie and G. S. Young, *Laboratory Investigation*, 2012, 92, 1492-1502.

245. J. L. Suhalim and E. Potma, in *Ex-vivo and In-vivo Optical Molecular Pathology*, Wiley-VCH Verlag GmbH & Co. KGaA, 2014, pp. 103-146.